TEKTONIKA

Constrictional Flow and Strain Partitioning During Oblique Deformation: Insights From the Variscan Tanneron Massif, SE France

Josselin Gremmel *[1], **Guillaume Duclaux** [1,2], **Michel Corsini** [1], **Jérôme Bascou** [3]

[1]Université Côte d'Azur, CNRS, Observatoire de la Côte d'Azur, IRD, Géoazur, 250 rue Albert Einstein, Sophia Antipolis 06560 Valbonne, France | [2]School of Earth Sciences, The University of Western Australia, Perth, WA, Australia | [3]Université Jean Monnet, CNRS, LGL-TPE UMR5276, F-42023, Saint-Etienne, France

Abstract Structural analysis through precise digital mapping combined with microstructural and quantitative finite strain data were used to investigate strain partitioning and strain shape evolution during the late-stage oblique tectonic collapse of a hot orogen. The Tanneron Massif in SE France was structured in an oblique tectonic regime at the end of the Variscan orogeny, leading to the exhumation of lower to middle crustal migmatite terranes. Strain patterns show prominent stretching lineations associated with L>S tectonites and dextral strike-slip shear zones compatible with subsimple shear deformation. The overall kinematics, with pure shear sub-horizontal constrictional flow and sub-vertical simple shear-dominated transcurrent corridors, depict a transtensional regime. The progressive transtensional deformation event evolves through two successive intermediate phases. The first phase is characterised by dominant sub-horizontal flow of the ductile crust represented by gently dipping foliation and L>S tectonites associated with widespread sub-horizontal stretching lineations. The second involves plane strain flow associated with vertical foliation and S-L tectonites. Finite strain analysis confirms the monotony of the L>S and S-L tectonites and highlights a partly lithological control on the finite strain ellipsoid shape with meta-igneous units defining L>S fabrics while meta-sedimentary units depict S-L fabrics. Microstructural observations also constrain the temperature evolution of the progressive transtensional deformation. Sub-horizontal flow starts at supra-solidus conditions and progresses to sub-vertical shear down to greenschist facies solely in hydrated meta-sedimentary units. We propose a rheologically driven strain path partitioning during the progressive exhumation of this deep crust throughout a two-phase transtensional regime.

Executive Editor: **Graeme Eagles**
Associate Editor: **Kim Welford**
Technical Editor: **Mohamed Gouiza**

Reviewers: **Aude Gébelin**
Anonymous

Submitted: **9 June 2023**
Accepted: **16 July 2024**
Published: **17 October 2024**

1 Introduction

Oblique tectonic systems, characterised by the combination of strike-slip and compressional or extensional components, are widespread on Earth and have become more commonly described as our understanding of geologic structures advances (*Dewey*, 2002; *Dewey et al.*, 1998; *Fossen and Tikoff*, 1993, 1998; *Harland*, 1971; *Oldow et al.*, 1990; *Sanderson and Marchini*, 1984; *Teyssier and Tikoff*, 1999). These systems, including their end-members transpression and transtension, have been extensively studied in the brittle crust, focussing on seismic implications and specific structures such as pull-apart basins, en-echelon folds, and fault arrays (*Alvarado et al.*, 2011; *Asti et al.*, 2022; *Brune*, 2014; *Chorowicz and Sorlien*, 1992; *De Paola et al.*, 2005; *Duclaux et al.*, 2020; *Ferranti et al.*, 2009; *Meghraoui and Pondrelli*, 2013; *Morley et al.*, 2004; *Norris et al.*, 1990; *Richard et al.*, 1995; *Schreurs and Colletta*, 1998; *Umhoefer and Dorsey*, 1997; *Wilson et al.*, 2006; *Withjack and Jamison*, 1986). At the plate boundary scale, the San Andreas fault in California (*Sylvester and Robert*, 1976; *Teyssier and Tikoff*, 1998), the Alpine fault in New-Zealand (*Cashman et al.*, 1992; *Teyssier et al.*, 1995) and the Great Sumatran faults in Sumatra (*Mount and Suppe*, 1992; *Tikoff and Teyssier*, 1994) represent some of the most closely studied examples of oblique plate motion worldwide. However, research on oblique tectonics in the ductile domain of the middle to lower crust reveals structural complexity that makes interpretation of fabrics challenging (*Archanjo et al.*, 2002; *Bascou et al.*, 2013; *Chardon et al.*, 2009, 2011; *Clegg and Holdsworth*, 2005; *Faleiros et al.*, 2022; *Gapais et al.*, 2008; *Gébelin et al.*, 2007; *Klepeis et al.*, 2022; *Paulsen et al.*, 2004; *Wiest et al.*, 2019), especially in the context of hot orogens. These studies, which are mainly confined to Precambrian orogens, remain scarce in Phanerozoic systems, and focus mostly on strain analysis within the transpressional regime. Transtension remains poorly understood and yet it is

*✉ gremmel@geoazur.unice.fr

expected to play a key role during orogenic collapse (*Dewey*, 2002) in order to progressively thin orogens.

In this study, we aim to provide a detailed description of strain shape and partitioning evolution within an oblique tectonic regime in the context of late-stage evolution of a Phanerozoic hot orogen. We investigate the development of crustal fabrics formed by oblique tectonic flow in the Variscan belt, exposed in the most internal part of the Maures-Tanneron Massif of SE France. By combining structural analysis through detailed field mapping, microstructural observations, and finite strain and tectonite calculations, we define the three-dimensional kinematic framework of transtensional flow in the Carboniferous basement of the Tanneron Massif.

Our results show that widespread gently dipping constrictional fabrics associated with vertical strike-slip shear zones are produced in transtension. In detail we observe two distinct strain patterns, defined by different tectonic fabrics and contrasting deformation temperatures, and show their distribution to be lithologically controlled. We propose that strain partitioning and localisation are partly controlled by rheological contrasts between ortho- and paragneisses during exhumation and retrograde deformation. Orthogneiss units preferentially preserve the initial high-temperature constrictional phase, while the subsequent lower-temperature strike-slip phase is preferentially localised in the weaker paragneiss units. This study contributes to a better understanding of the complex processes and structures involved in oblique tectonic regimes within ductile crustal environments. The described tectonic evolution represents a good example of the kinematic framework developed during exhumation of the internal part of a collapsing orogen.

2 Geological Setting

2.1 Maures-Estérel-Corsica-Sardinia (MECS) Microplate

The Maures-Tanneron-Massif (MTM) represents the southernmost segment of the Variscan belt in mainland France whose development has been related to the evolution of the Maures-Estérel-Corsica-Sardinia (MECS) microplate (*Edel et al.*, 2018). The Corsica-Sardinia block rifted apart from the MTM block during Miocene Mediterranean back-arc extension that involved a 45–55° anticlockwise rotation (*Gattacceca*, 2000). Along the Mediterranean coast, the MTM extends from Toulon in the southwest to Cannes in the northeast, forming a 90 km long and 50 km wide belt (Figure 1).

The MTM is defined as a subduction-collision belt that was active from 420 to 300 Ma (Schneider et al., 2014). After the subduction event, a 360-330 Ma collisional stage (*Oliot et al.*, 2015; *Schneider et al.*, 2014) was responsible for structuration of the MTM into N-S litho-tectonic units following an increasing metamorphic gradient from west to east (*Rolland et al.*, 2009). Metamorphic isograds progress from the chlorite zone, via the garnet-chlorite, biotite-staurolite, and biotite-kyanite zones, to the biotite-muscovite-sillimanite zone (*Buscail*, 2000). Based on this, the belt is divided in two domains: the external domain of low grade metamorphic rocks in the west, and the internal domain to the east, which is composed of migmatitic units (Figure 1). At the end of the collisional stage, a first partial melting event with associated calc-alkaline magmatism is documented at 340-330 Ma (*Oliot et al.*, 2015). Within the internal domain, a gneiss dome structure is juxtaposed with the Rouet granite intrusion and associated with pervasive vertical strike-slip shear zones, which have been dated to between 325 and 300 Ma. These observations have been interpreted as the results of a regional transpressive stage marking the waning of the orogenic cycle (*Corsini and Rolland*, 2009; *Rolland et al.*, 2009). This late deformation event has largely overprinted preexisting fabrics. In Sardinia, the event has also been dated to between 320 and 300 Ma (*Carosi et al.*, 2012). At the scale of the MECS microplate, the oblique deformation is mostly interpreted as having occurred in a transpressional regime (MTM: *Rolland et al.*, 2009; *Simonetti et al.*, 2020a; Sardinia: *Carosi et al.*, 2012; *Frassi et al.*, 2009), while some authors described evidence for a transtensional setting (MTM: *Buscail*, 2000; Corsica: *Thevoux-Chabuel et al.*, 1995). Widespread granitoid and related dykes were emplaced synchronously with this late event in the MTM (*Bolle et al.*, 2023; *Corsini et al.*, 2010; *Duchesne et al.*, 2013).

At the close of the Variscan cycle, thinning and exhumation of the migmatitic units accompanied the opening of late Carboniferous pull-apart basins along major north-south crustal shear zones (SZ) (Figure 1): the Plan-de-la-tour Basin along the Grimaud SZ (*Onézime et al.*, 1999) and the Reyran Basin along the La Moure SZ (*Toutin-Morin et al.*, 1994). These narrow N-S intramontane half graben basins consist of folded coarse detrital sediments eroded from the surrounding migmatitic units, alternating with lignite layers (*Maillet et al.*, 2021). These basins are thought to have opened and filled between 315 and 298 Ma (*Toutin-Morin et al.*, 1994), synchronously and parallel to the development of the basement fabrics. Folding and faulting are pre-Permian (*Toutin-Morin et al.*, 1994). East-west oriented Permian grabens opening perpendicular to the late-Variscan fabrics seal the MTM cycle (Figure 1). These Permian intracontinental sediments and associated volcanics witness a short-lived rifting episode and are responsible for splitting the MTM into two distinct massifs, the Maures and Tanneron (*Toutin-Morin et al.*, 1994). Triassic continental deposits unconformably overlay the MTM and Permian sequence and mark the base of the thrusted Alpine-folded Mesozoic cover sequence that bounds the MTM to the north.

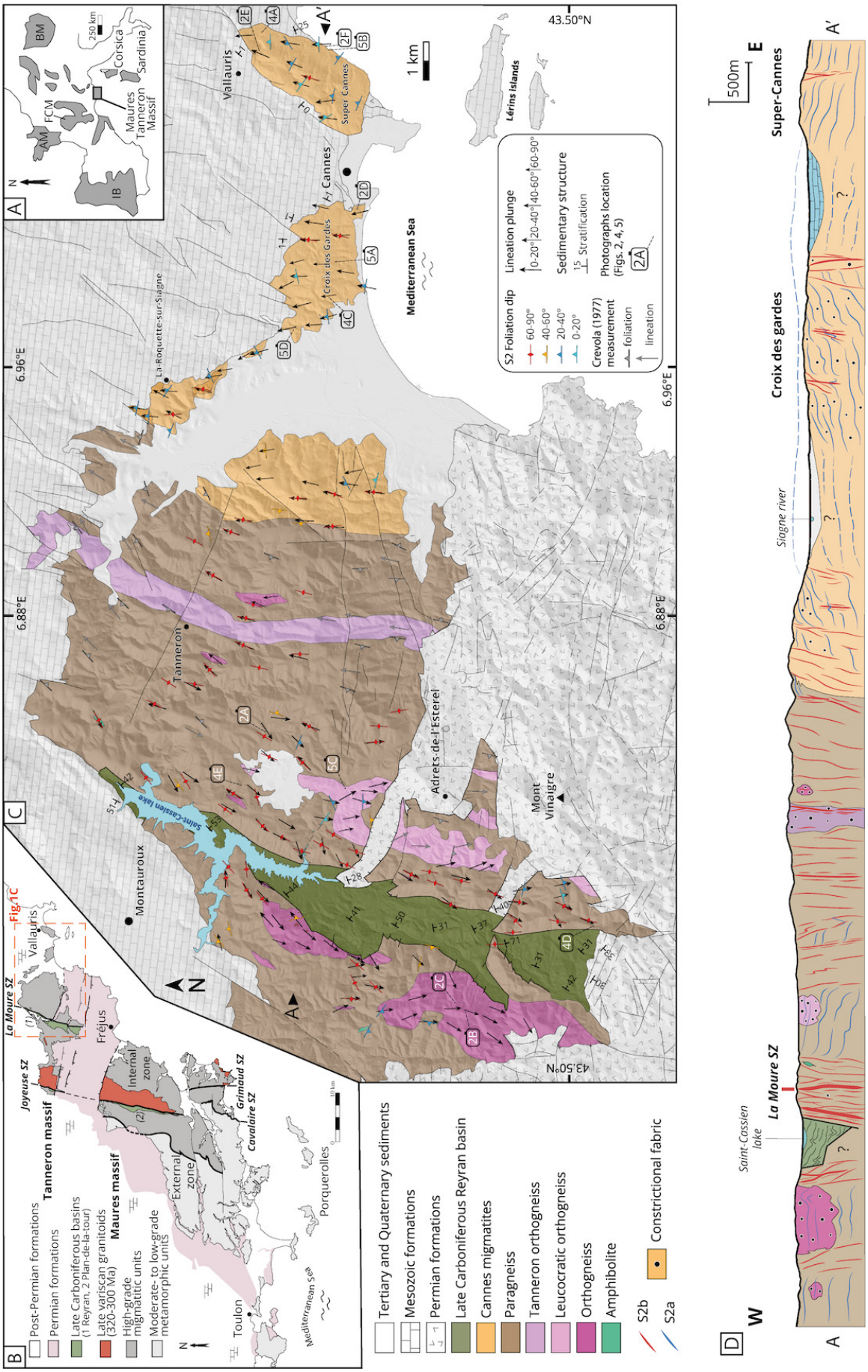

Figure 1 – **(A)** Location of the Maures-Tanneron Massif in western Europe with main Variscan massifs (IB: Iberian Massif, AM: Armorican Massif, FCM: French Central Massif, BM: Bohemian Massif) (modified from *Gerbault et al.*, 2018). **(B)** Simplified tectonic map of the Maures-Tanneron Massif. **(C)** Geological map of the eastern Tanneron. Location of the A-A' cross section below is indicated on the map. **(D)** Schematic cross section of the eastern Tanneron.

2.2 Eastern Tanneron Massif

The study area is located in the Tanneron Massif at the easternmost part of the MTM and thus belongs to the belt's innermost domain (Figure 1). The Tanneron Massif is exposed along a 40 km E-W trending band bounded by the Mediterranean Sea and Permian deposits to the south and Alpine Mesozoic cover to the north, and partially overlaid by the Tertiary-Quaternary Siagne alluvial deposits. This massif consists of a migmatised metasedimentary sequence with abundant metre- to kilometre-long orthogneiss bodies (*Crevola*, 1977; *Orsini*, 1968), and hosts the Carboniferous Reyran Basin. Few studies have focused on the Eastern Tanneron Massif. As such, we present lithological descriptions based on our personal field observations.

The migmatitic paragneisses are the dominant lithology of the area. They occur as dark stromatic metapelites (Figure 2A) with a Qtz+Kfs+Pl±Bt±Ms±Chl assemblage and rare garnet, apatite, and tourmaline. Stable sillimanite and relict kyanite can also be found. The migmatites are all metatexites, although proportions of leucosome and melanosome vary, leading to different paragneiss facies. They host lenses of orthogneiss, mica schist, layered amphibolite, quartzite, marble, and calc-silicate (Figure 1).

The migmatitic orthogneisses are mica-bearing leucocratic orthogneisses (Figure 2B) with rare thin leucosomes. Their granitic protolith was emplaced around 400 Ma (*Oliot et al.*, 2015). Individual bodies are compositionally homogenous, showing a texture of regularly alternating stretched trails of dominant quartz-feldspars and trails of biotite-muscovite (Figure 2B). The granitoid protolith remains visible in low strain zones (Figure 2C). Nevertheless, mineralogical variations are possible with several different facies and a diversity of fine variations is visible in the field between the orthogneiss and paragneiss, as already observed by *Orsini* (1968). The major difference between the para- and orthogneisses seems to be the homogeneity at the outcrop scale, the orthogneisses showing constant distributions of mineral trails while the paragneisses comprise alternating leucosome and melanosome bands of varying quantity and size.

To the east of the narrow Carboniferous Reyran Basin, the leucocratic orthogneiss unit represents an elongated body inside the larger migmatitic paragneiss (Figure 1). This unit is composed of a very fine grained highly stretched light gneiss, rich in quartz-feldspar with rare muscovite and garnet, and has been interpreted as a meta-rhyolite (*Crevola*, 1977; *Orsini*, 1968). Locally, different facies are associated with the leucocratic orthogneiss, mainly a darker medium grained orthogneiss.

Further east, the Cannes migmatite units are homogeneous ortho-derived Qtz+Kfs+Pl+Bt±Ms pale pink to pale yellow migmatites with minor garnet and apatite (Figure 2D). These ortho-migmatites are often micro-folded and show thick coarse grained leucosomes with centimetre-scale augen K-feldspar alternating with thinner biotite-rich melanosomes (Figure 2D). Stromatic migmatite fabrics are well preserved in this unit, with melts in leucosomes migrating toward the hinges of similar folds (Figure 2E) and leucosomes injected in shear bands. Variations in the degree of anatexis in the migmatite create local secondary facies, such as nebulite (Figure 2F).

Diverse granite and pegmatite veins emplaced within, or crosscutting, the migmatitic foliation are widespread in the area, highlighting the partial melting of the crust in this internal part of the MTM. The Cannes migmatites are crosscut by sharp granite veins meaning that deep partial melting persisted until the end of the orogenic cycle.

Despite the MTM's polyphase Variscan orogenic history, the protracted 325-300 Ma event has totally overprinted previous structures in the eastern Tanneron Massif. Structural data remain scarce in the area. The main previous work was done by *Crevola* (1977) in the east of the Reyran Basin ("oriental Tanneron"), describing four deformation phases with a major pervasive N-S foliation, "S2", defining large scale folds from the Reyran Basin to the Cannes eastern termination. A km-scale synform with symmetric limbs on each side of the Reyran Basin is followed by a large antiform with its eastern limbs ending around Cannes (*Corsini et al.*, 2010; *Crevola*, 1977). Stretching lineations plunge gently to the north or south (*Crevola*, 1977) and may be dominant over foliation locally to the west of the Reyran Basin (*Orsini*, 1968). The area is also structured by the crustal-scale, vertical, dextral, La Moure SZ on the east-side of the Reyran Basin (*Rolland et al.*, 2009). Ar-Ar muscovite ages in the range 320-310 Ma in the eastern Tanneron are interpreted to represent this late structuration of the massif (*Corsini et al.*, 2010).

3 Methodology

3.1 Field Mapping and Analysis

To investigate strain partitioning and evolution, we targeted the key Reyran and Cannes zones for detailed field mapping and analysis. The Reyran zone, located on both sides of the Carboniferous Reyran Basin (Figure 1), represents a crucial transition between the coeval basin opening and ductile basement deformation. The Cannes zone, located at the extreme east of the massif (Figure 1), represents the innermost part of the orogen, with ubiquitous migmatites displaying high-temperature fabrics. Exposure in this latter zone is separated into a group of three neighbouring hills: the Roquette-sur-Siagne, Croix des Gardes, and Super-Cannes hills (Figure 1). Both key areas were thoroughly investigated and sampled with the acquisition of more than 4500

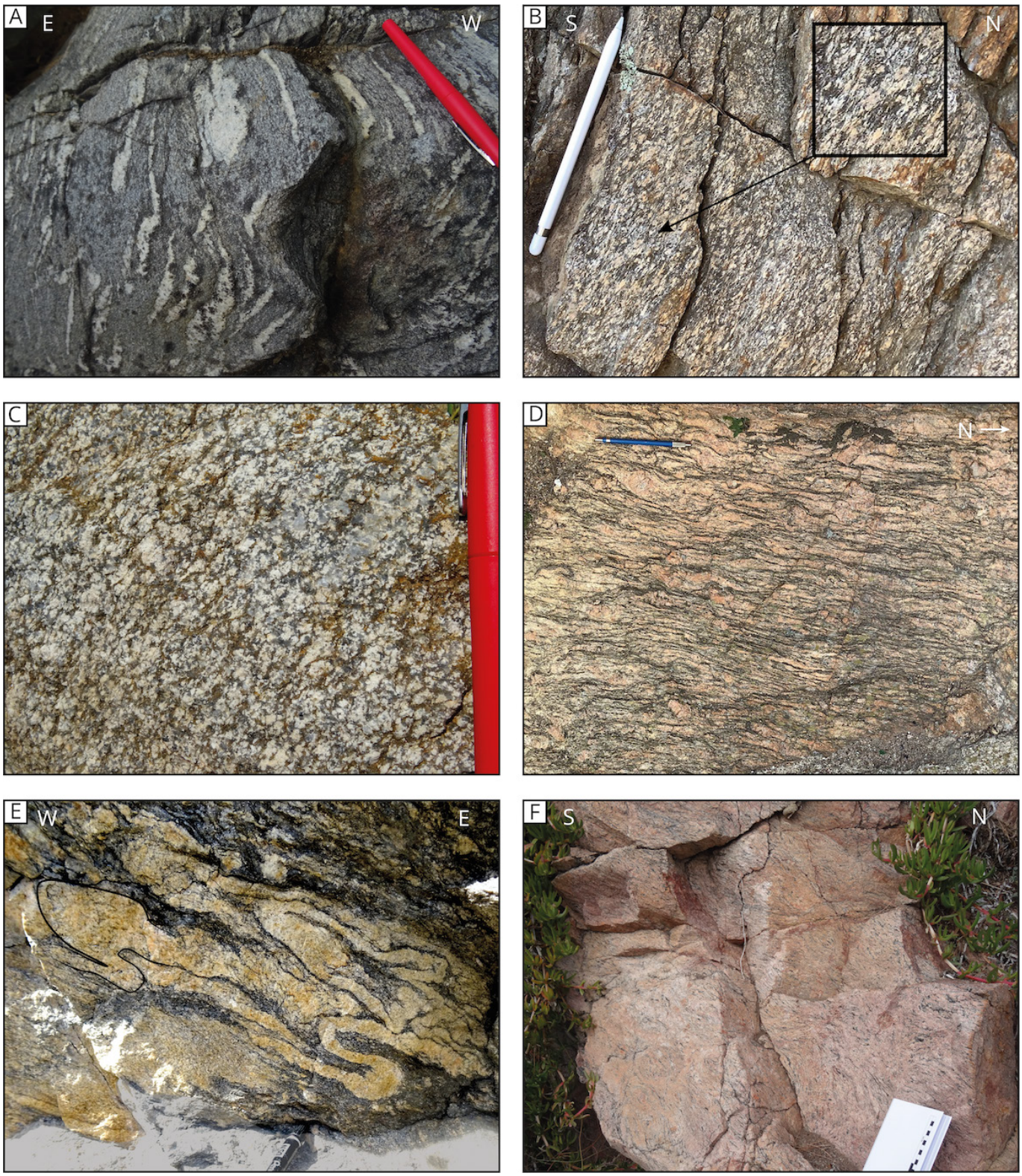

Figure 2 – Photographs of the migmatitic paragneiss and orthogneiss and Cannes migmatites, showing their main lithological and structural appearance in the field. **(A)** The migmatitic paragneiss is a dark stromatic metapelite with visible regular centimetric leucosomes in a low strain domain (GPS coordinates: lat/lon = 43.5711/6.8417). **(B)** The migmatitic orthogneiss commonly appears as a stretched micro-granite with a homogeneous texture of alternating lenses or bands of leucocratic quartz-feldspar and dark biotite-muscovite (Sample JG21-02, 43.5301/6.7465). **(C)** Granitoid protolith of the migmatitic orthogneiss (B) visible in a low strain local domain (lat/lon = 43.5354/6.7620). **(D)** The Cannes migmatite is a stromatic migmatite, defined by pale pink to pale yellow thick irregular and coarse grain leucosomes alternating with thinner dark melanosomes. Centimetric augen K-feldspars are visible in the leucosome layers (lat/lon = 43.5507/7.0108). **(E)** Migration of melt toward the hinge of similar folds in irregular leucosomes, indicative of high grade deformation synchronous with partial melting (Super-Cannes hill, lat/lon = 43.5732/7.0619). **(F)** Secondary facies of the Cannes migmatites with a higher degree of anatexis visible by the ubiquitous leucosomes over melanosomes, giving a nebulitic texture (lat/lon = 43.5584/7.0645). Outcrops locations are shown in Figure 1 for reference.

structural measurements. Field observations and measurements were acquired through digital mapping on an iPad-mini tablet with FieldMove software (Midland Valley). Observations and direct measurements were exported to a GIS software for data analysis and interpretation, and thematic map building. For each outcrop, foliations and/or lineations were systematically measured, and a qualitative estimate of the finite strain ellipsoid shape was given in the form of a tectonite classification scheme (S>L, S-L, L>S-tectonite) when outcrop quality was sufficient (see §3.2 below).

3.2 Qualitative Method: Tectonite-type Map

We built a qualitative tectonite-type map (see §4.4) showing three different symbologies corresponding to S>L, S-L, and L>S tectonites. For most outcrops, the tectonite type was gauged from direct field observations of the fabric geometries between the XZ and YZ planes. For others, tectonite type was attributed directly using GIS software following this classification: Outcrops where only a flattening plane foliation was identified and measured have been classified as S>L, outcrops where both a foliation and mineral or stretching lineation was identified have been classified as S-L, and outcrops where only mineral or stretching lineation was identified have been classified as L>S.

3.3 Quantitative Methods: Microstructural Ellipse Measurement and Anisotropy of Magnetic Susceptibility (AMS)

To validate the qualitative observations, we used two quantitative methods: microstructural ellipse measurement and anisotropy of magnetic susceptibility (AMS). 3D finite strain ellipsoids were calculated based on microstructural observations for 20 oriented samples. These samples were cut along and across the main foliation and/or lineation in order to produce two thin sections parallel (XZ plane) and perpendicular (YZ plane) to the principal finite strain axis. We acquired high-resolution scans of the whole thin sections. Then, we used EllipseFit software version 3.8.2 (*Vollmer*, 2018) to calculate statistical ellipsoid parameters by identifying and drawing ellipses in the scans. The Fry technique was not used because Fry's starting hypothesis implies that the reference objects were of uniform size and homogeneously distributed before deformation. In the migmatitic units, leucosomes were often targeted as reference objects because of their homogeneous composition and as they represent a good marker of finite deformation of the rocks in sub and supra-solidus conditions. Mean ellipse factors were obtained by digitising polygonal leucosome shapes from the thin section scans and then converting them to ellipses with the "Shape" method of EllipseFit. Following this, the mean 2D ellipse factors from thin sections parallel and perpendicular to the stretching axis are gathered to reconstitute the mean 3D ellipsoid factors of the sample with the Shan method (*Shan*, 2008). The resulting ellipsoid parameters are compiled (Table 1) and plotted in a Flinn diagram to visualise the shape and intensity of finite strain for each sample.

For the AMS study, 75 oriented cores were sampled using a gasoline-powered portable drill at 5 sampling sites in paragneiss and orthogneiss of the Reyran zone. Four sites follow a broad E-W cross-section in the La Moure SZ and one site is located in the major orthogneiss body of the west side of the Reyran Basin. The cores were cut in the laboratory (see below) in specimens of standard paleomagnetic size. The AMS was measured using a MKF1 Kappabridge at the University of Saint Etienne, LGL-TPE laboratory (France) and data were processed using the ANISOFT package of programs (AGICO, Inc). Coupling a CS4 furnace to the MFK1 Kappabridge allowed for thermomagnetic measurements to constrain the magnetic mineralogy. The AMS data are represented by three main parameters: Km, Pj, and T. The Km parameter is defined by Km = (K1+K2+K3)/3 as the mean bulk magnetic susceptibility, where $K1 \geq K2 \geq K3$ are the three principal susceptibility axes of the AMS ellipsoid. Following the magnetic fabric, K1 (Kmax) depicts magnetic lineation and K3 (Kmin) denotes a pole to magnetic foliation. The Pj parameter is the corrected degree of anisotropy, which represents the intensity of the magnetic fabric as a reflection of the eccentricity of the AMS ellipsoid. The T parameter of *Jelinek* (1981) defines the shape of the AMS ellipsoid, which ranges between -1 (prolate ellipsoid) and 1 (oblate ellipsoid).

3.4 Use of Tectonic Terms 'Event' - 'Stage' - 'Phase'

Our model defines the tectonic evolution by two successive deformation phases during a single tectonic event in contrast to two separated different tectonic events. Hence the "phases" represent deformation increments in our study area which are not to be confused with "events" or "stages" defined by major changes in external (boundary) conditions. These former terms merely relate to local changes in strain accommodation as structures evolve (*Fossen et al.*, 2019).

4 Structural Architecture and Strain Pattern

4.1 Planar Fabrics

The planar deformation pattern is separated into two sets of fabrics, a low strain sub-horizontal S2a foliation and a higher strain sub-vertical S2b foliation (Figure 1 and 3). Although an older S1 foliation is evidenced by the preservation of rare isoclinal folds within the S2a domains, its continuity cannot be mapped.

Table 1 – Finite strain ellipsoid data (Microstructural Ellipses Measurement and corresponding AMS). Max(X), Int(Y), and Min(Z) represent the three principal axes of the finite strain ellipsoids.

Sample/ AMS site	GPS coordinates (lat/lon)	Lithology	Foliation (dip-dip) - S2a/b	Lineation	Field tectonite type	Microstructural ellipses measurement				AMS	
						Max (X)	Int (Y)	Min (Z)	Ellipsoide shape	T	Ellipsoide shape
JG20-01	43.5824/6.8167	Paragneiss	297/79 - S2b	223/13	S-L	1.902	0.992	0.53	S-L		
JG20-02	43.5825/6.8167	Paragneiss	280/80 - S2b	207/06	S-L	1.914	0.966	0.541	S-L		
JG20-03	43.5783/6.8190	Orthogneiss	161/73 - S2b	240/14	S-L	1.642	0.964	0.632	S-L		
JG20-04	43.5746/6.8294	Orthogneiss	129/47 - S2a	192/33	L>S	3.244	0.968	0.318	S-L		
JG20-05	43.5523/6.8240	Orthogneiss	/	175/04	L>S	2.825	0.689	0.514	L>S	-0.2 - 0.3	S-L
JG20-06	43.5579/6.8138	Paragneiss	242/38 - S2a	176/16	S>L	1.392	1.153	0.623	S>L	0 - 0.7	S-L / S>L
JG20-07	43.5119/6.7877	Orthogneiss	93/35 - S2a	166/07	L>S	3.905	0.757	0.338	L>S		
JG20-08	43.5354/6.7671	Paragneiss	200/62 - S2b	240/35	S-L	2.738	0.967	0.378	S-L		
JG20-09	43.5355/6.7663	Paragneiss	212/66 - S2b	257/43	S-L	2.385	0.891	0.47	S-L		
JG20-11	43.5454/6.8252	Orthogneiss	168/16 - S2a	166/17	L>S	2.927	0.619	0.552	L		
JG21-02	43.5301/6.7465	Orthogneiss	/	162/43	L	2.56	0.804	0.486	L>S	-0.2 - 0.4	S-L
JG21-03	43.5169/6.7543	Orthogneiss	/	209/27	L	2.826	0.61	0.58	L		
JG21-05A	43.5119/6.7877	Paragneiss	279/51 - S2a	02/03	L>S	2.3	0.858	0.507	L>S		
JG21-12	43.5384/6.7949	Orthogneiss	268/62 - S2b	209/33	L>S	1.378	0.872	0.832	L		
JG21-15	43.5612/6.7782	Orthogneiss	/	82/05	L	3.044	0.616	0.533	L		
JG21-16	43.5355/6.7617	Orthogneiss	/	215/11	L	2.627	0.685	0.556	L		
JG21-17	43.5816/6.9591	Cannes migmatite	/	355/37	L	2.132	0.694	0.676	L		
JG21-19	43.5669/6.9722	Cannes migmatite	/	347/20	L	2.177	0.752	0.611	L		
JG21-20	43.5616/6.9808	Cannes migmatite	/	13/28	L	3.694	0.679	0.399	L>S		
JG21-21	43.5568/7.0047	Cannes migmatite	261/89 - S2b	353/14	S-L	3.165	0.898	0.352	S-L		

The S2a fabric trends approximately E-W and dips gently (0-40°) to the north in the Cannes zone and to the south in the Reyran zone (Figure 4A). Overall, however, kinematic indicators in both the east and west highlight top-to-the-south movements (Figure 4B). However, asymmetric criteria are scarce and fabrics are mainly coaxial pointing to dominantly pure shear kinematics. Despite the overall E-W strike, the S2a foliation shows local variations due to late folding which are represented by small irregular curves on the foliation trajectory (Figure 3). The S2a trend direction is not well constrained in the southwestern part of the Reyran zone and in some parts of the Croix des Gardes hill where foliations are missing and only lineations are measurable. Around the Reyran Basin, S2a is restricted to narrow preserved patches surrounded by anastomosed corridors with S2b foliation (Figure 3A). S2a is more visible in the Cannes migmatites and orthogneiss lithologies than in the paragneisses. In the Cannes zone, S2a is well developed and predominates over S2b. The Super-Cannes hill (Figure 3D) is mostly defined by gently dipping S2a foliations (0 to 20°) (Figure 4A) and exhibits complex foliation patterns with a vague NW-SE trend locally deflected by hectometre-scale domal shapes at the origins of triple junctions causing high variability in trend directions. The main strike direction is approximately NW-SE but E-W, N-S and NE-SW directions are also observed (Figure 3D). These heterogeneous directions are highlighted by foliation triple points and a concentric half-dome structure in the west part of the hill. S2a foliation is overprinted by the S2b vertical foliation, as illustrated by the S2a deflection at the contact with the La Moure SZ, especially in the south of the SZ (Figure 3A). Locally, S2a foliation is folded and transposed along subvertical S2b planes (Figure 4C).

Although S2b foliation is pervasive in the whole study area, it is far better developed in the paragneisses than the orthogneisses or Cannes migmatites. S2b foliation trends N000 to N020 with sub-vertical (60-90°) dips (Figure 3) and its occurrence is associated with high strain zones defined by SL fabrics. This plane strain deformation is associated with strike-slip kinematics forming widespread metre- to kilometre-scale SZs that are especially concentrated on the eastern side of the Reyran Basin. The La Moure SZ, the biggest and most representative of these features, consists in a 1 km-wide anastomosed network of vertical foliations bounding the eastern side of the Carboniferous Reyran Basin along a roughly N015-020 trend (Figure 3A). Mylonitic paragneiss in the SZ has a dark recrystallised fine-grained matrix into which sheared leucosomes are transformed into disrupted and stretched lenses, or separated into trails of clasts (Figure 4D). Ultramylonites are also observable in the paragneiss with >90% recrystallised matrix and millimetre-to-centimetre-scale rounded pearls of leucosomes. The main kinematic sense of the La Moure SZ is dextral (Figure 3), which is visible through a preponderance of dextral S/C structures, asymmetric leucosome sigmoids, drag folds, and mica fish (Figure 4E,F). Sinistral indicators are also present locally. Deflection of the S2a foliation against the La Moure SZ also indicates mostly sinistral kinematics (Figure 3). Previous authors described complex kinematics for the main transcurrent SZs of the MTM and Sardinia, and suggest successive phases of dextral and sinistral kinematic movements (*Bellot*, 2005; *Buscail*, 2000; *Carosi et al.*, 2012; *Vauchez and Bufalo*, 1988). An east to west strain gradient is observable within the La Moure SZ evolving from mylonites in the east to ultramylonites near the border of the Reyran Basin.

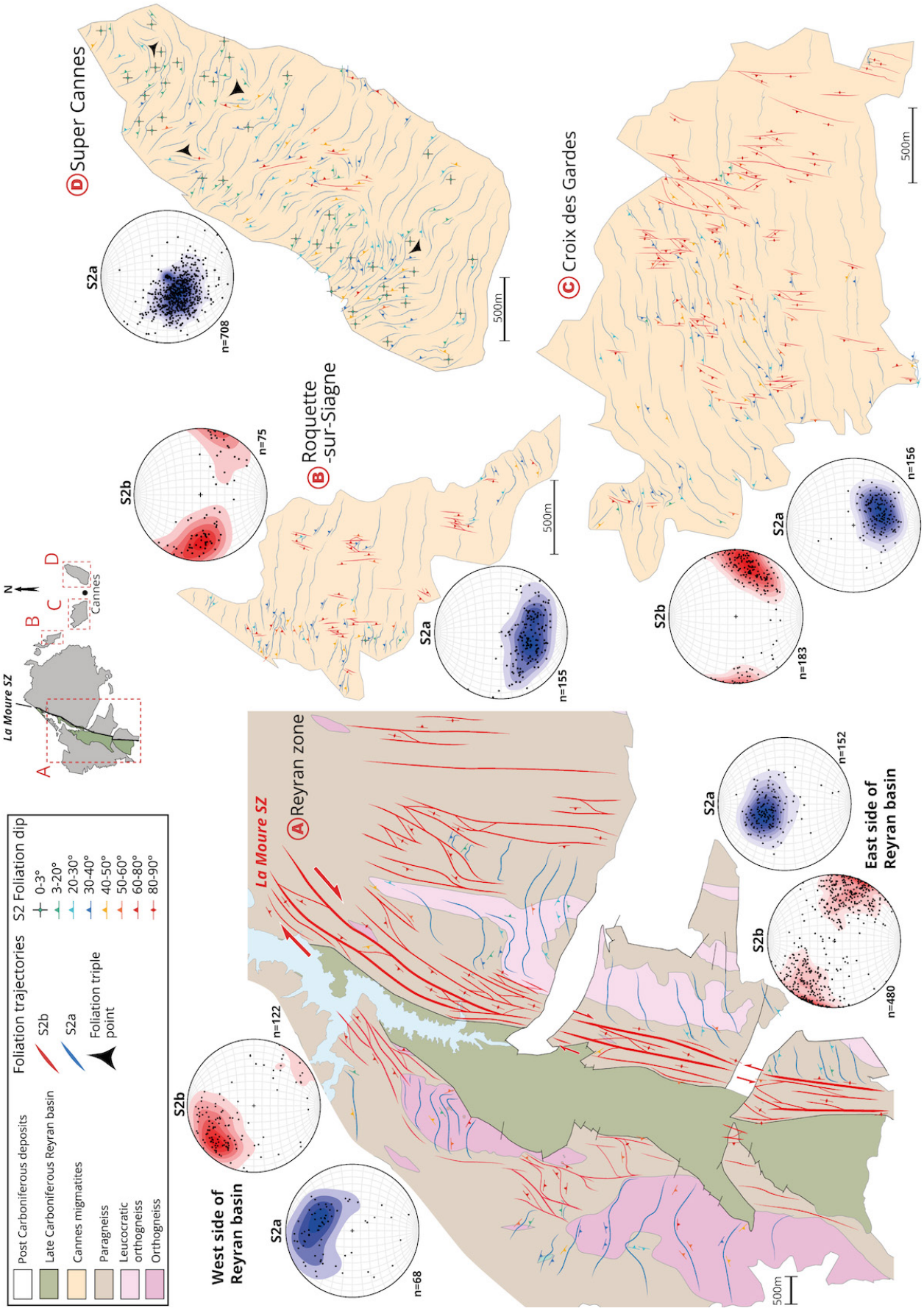

Figure 3 – Structural maps showing foliation trajectories and highlighting the two strain patterns for the Reyran zone and the three Cannes hills. Lower hemisphere stereograms of foliation poles for the two planar fabrics S2a and S2b are given close to their respective areas. See the anastomosed network of the vertical La Moure SZ (S2b foliations) bounding the eastern side of the Reyran Basin and which overprints S2a foliations as emphasised by the deflection of S2a foliation close to the SZ. The Super Cannes hill reveals highly variable S2a orientations highlighted by the presence of foliation triple points and a concentric half-dome pattern in the western part.

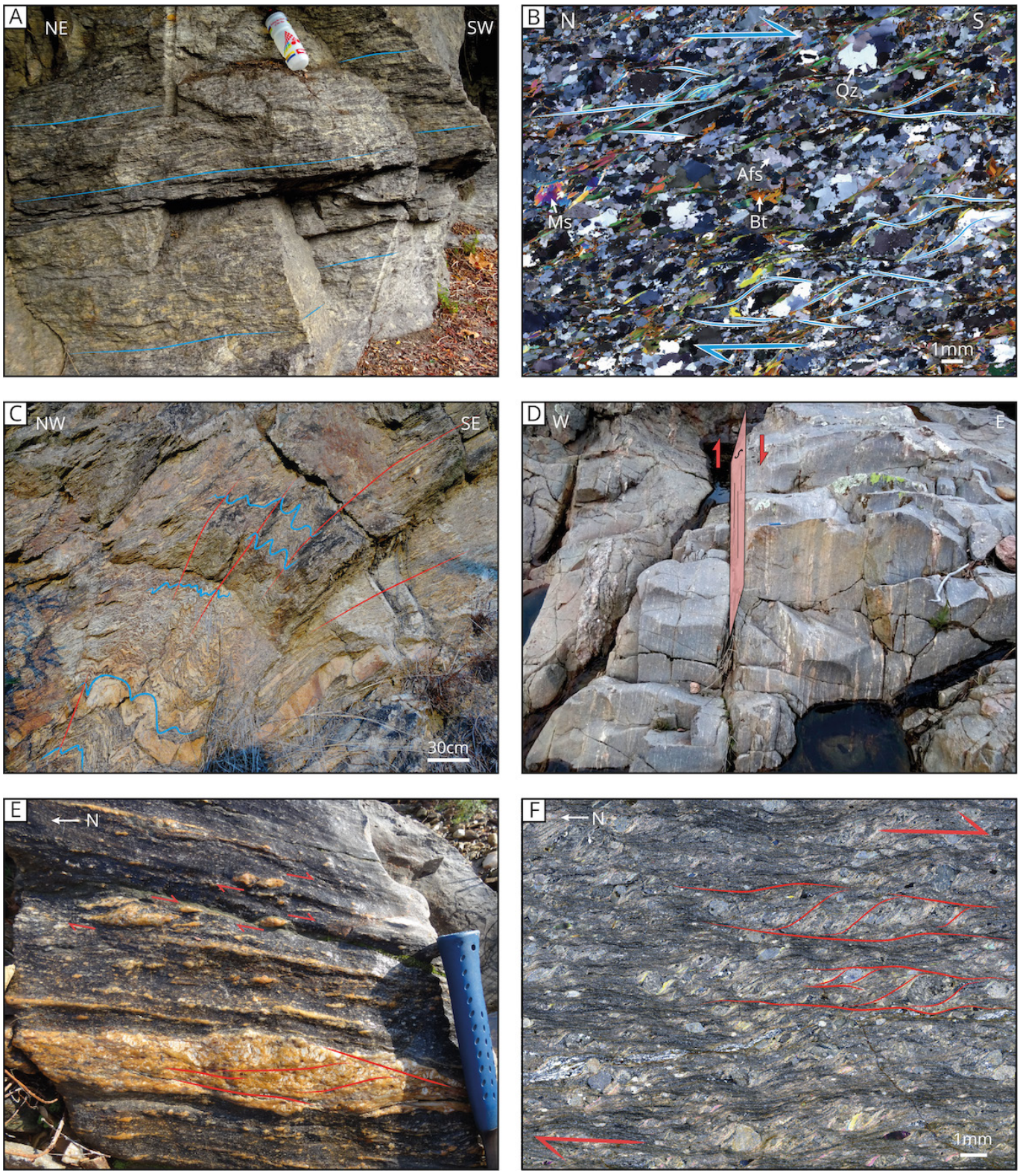

Figure 4 – Geometry and kinematics of the main planar fabrics. **(A)** Low strain flat-lying foliation representative of S2a foliation, here in the Super Cannes hill (GPS coordinates: lat/lon = 43.5725/7.0678) - 3D model visible here: https://skfb.ly/oQIrH. **(B)** Microphotograph of a migmatitic orthogneiss in the Reyran zone displaying top to the south S/C shear structures (lat/lon = 43.5300/6.7462). **(C)** S2a foliation folded and transposed by S2b foliation, in the Croix des Gardes hill (lat/lon = 43.5571/6.9842). **(D)** Representative outcrop of the La Moure SZ (and other smaller SZ) showing vertical strike-slip mylonitic S2b foliation in the migmatitic paragneiss (lat/lon = 43.4954/6.7808). **(E)** Kinematic indicators giving a dextral sense of shear in mylonitic paragneiss from the La Moure SZ (lat/lon = 43.5758/6.8274). **(F)** Microphotograph of an ultramylonitic paragneiss of the La Moure SZ near the contact with the Reyran Basin. The texture of the highly recrystallised matrix defines widespread S/C shear bands indicating dextral kinematics. See the intense grain size reduction down to micrometric scale for this ultramylonite due to very high strain deformation at the contact with the Reyran Basin (lat/lon = 43.5412/6.7935). Outcrops locations are shown in Figure 1 for reference.

The basin-bounding ultramylonites are often also deformed under brittle conditions, showing fracture networks. In the Cannes zone, the S2b foliation is distributed in small scattered N-S vertical corridors inside the dominant E-W S2a foliation.

The entire structure is folded (in association with the development of S2a and S2b foliations) at scales that range from centimetres to decametres depending on the lithological units. The Cannes migmatites are highly micro-folded (Figure 5A) and show regular metre- to decametre-scale cascading folds (Figure 5B) while other units appear less folded and show mainly localised decimetre-scale folds. Folds plunge at between 10 and 30°, towards the north in the Cannes zone (N340-020) and south in the Reyran zone (N180-210), everywhere parallel to the local stretching lineation (L2), a common feature of oblique tectonics (Figure 6). A few steeply dipping fold axes, plunging at around 60-70°, are also visible locally in the Croix des Gardes hill and Reyran zone. Axial planes are oriented mainly parallel to the surrounding foliation, nearly E-W in the S2a foliation domain and close to N-S in the S2b foliation domain. In the Reyran zone, folds are close to tight and most of the time symmetric and concentric, whereas folds in the Cannes zone are more diverse and disorganised. Most of the micro-folded structures in the Cannes zone are close to tight and symmetric but decimetre- to metre-scale folds may also be gentle to open, asymmetric and/or similar folds. Some of these gentle to open folds are not considered as tectonic and could be interpreted as resulting from the natural buoyant flow of this migmatitic hot and soft unit.

4.2 Linear Fabrics

L2 mineral and stretching lineations are ubiquitous and represent a major feature of the structural pattern of the Tanneron Massif. These lineations are represented by stretched leucosomes and melanosomes, elongated quartz rods, and mica trails. Unlike the planar fabrics, L2 lineations present a homogeneous and consistent structural pattern throughout the whole area. This is a common feature in the MTM, at least for the internal domain of the Maures Massif (*Bolle et al.*, 2023). Thus, the L2 lineations form a single set and are systematically associated with both the S2a and S2b foliations. L2 linear fabrics are described by N-S directed sub-horizontal stretching lineations that mainly dip at between 10 and 30° (Figure 6). The stretching lineations transect continuously all the lithological units and their contacts without variation, showing that the entire area was deformed in the same tectonic regime. The plunge direction changes from north in the east of the area to south in the west (Figure 6). In detail, plunge directions range between N340-N030 in the eastern part of the study area and N230-N160 in the western part, and show curved trajectories that converge or diverge (Figure 6). L2 lineations oriented at high angles to the mean N-S direction (N240-250) can be observed locally in the west and east of the Reyran Basin. Around the basin, lineations are mostly oblique to the La Moure SZ, which represents the reference for simple shear flow. In detail, the main direction of the La Moure SZ is N015-020, while L2 lineations follow two main directions, N220 and N165, lying at mean angles of 20-30° to the SZ.

In many places, the L2 lineation is the main structural feature, defining the rock fabric and outcrop architecture. Usually, stretching lineations present a dominant continuous direction while foliations are much more variable, their strikes and dips evolving by folding around the axes of the lineations. The predominance of L2 stretching lineations over flattening foliation planes is visible in these rocks up until the development of L>S tectonites. In fact, especially away from the S2b corridors, it is common to find outcrops where foliation is weak to non-recognisable in the face of the robust stretching L2 lineation, even up to the point where only lineation fabric is visible (Figure 5C,D). In three dimensions, at outcrop scale as well as in thin section, these L>S tectonites present cigar-shaped structures with leucosome trails or quartz rods that appear highly elongated in the XZ section and rounded in the perpendicular YZ section (Figure 5D and E-F).

4.3 Finite Strain Shape

The major sub-horizontal to gently dipping stretching flow in the area leads more readily to the development of L>S and subordinate S-L tectonites than S>L-tectonites (Figure 7). Flattening strain is mostly restricted to the Super-Cannes hill (Cannes migmatite unit) where flat-lying foliations are frequently seen without any associated lineation and show similar deformation degree between the XZ and YZ planes (Figures 4B and 7). S-L-tectonites, representing plane strain fabrics, are widespread in the whole area and mainly along the S2b sub-vertical foliation, especially inside the La Moure SZ (Figures 3 and 7). Constriction (L>S type tectonite), following the gently dipping L2 lineation direction, whilst very common, is more prevalent in the E-W S2a foliation zones. Constriction is mostly observable in the orthogneiss units and the Croix des Gardes and Roquette hills of the Cannes migmatite (Figure 7), suggesting a lithological control on its preservation. In the field, these areas are marked by the occurrence of L-type tectonites displaying spectacular leucosome rods, highly stretched along the X-axis and wrapped around by micas along the orthogonal YZ plane (Figure 5C,D). No consistent foliation is observed on the YZ plane. The various meta-igneous units present a remarkable contrast with the migmatitic paragneiss. In fact, the transitions between migmatitic ortho- and paragneisses are consistently marked by the appearance of a highly developed stretching L2 lineation in the place of foliation.

Figure 5 – Geometry of folds, linear fabrics and finite strain shape. **(A)** Microfolds with axes parallel to the stretching lineation (L2) in the Cannes migmatite (Croix des Gardes, GPS coordinates: lat/lon = 43.5552/6.9908) - 3D model visible here: https://skfb.ly/oQK6o. **(B)** Cascading open fold with a representative right angled geometry in the Cannes migmatite (Super Cannes, lat/lon = 43.5550/7.0615) - 3D model visible here: https://skfb.ly/oQIqR. **(C)** L type tectonite in the leucocratic orthogneiss of the Reyran zone. See the absence of clear fabric in the section perpendicular to the stretching lineation (L2) (lat/lon = 43.5528/6.8234). **(D)** L type tectonite in the Cannes migmatite near the Croix des Gardes hill. See the rounded shape of K-feldspars and leucosome layers encircled by biotite rims in the section perpendicular to the dominant stretching lineation (L2) (Sample JG21-19, lat/lon = 43.5669/6.9722) - 3D model visible here: https://skfb.ly/oQIpy. (E-F) Thin section scans of the L-type migmatitic orthogneiss sample JG21-15, with **(E)** XZ section parallel to the stretching lineation (L2) and **(F)** YZ section perpendicular to the lineation. Examples of ellipses outlined with the Ellipsfit software are shown, used for 3D finite strain ellipsoid calculation (see Methodology section). See the differences in fabrics and elliptical shapes between both sections (lat/lon = 43.5612/6.7782). Outcrops locations are shown in Figure 1 for reference.

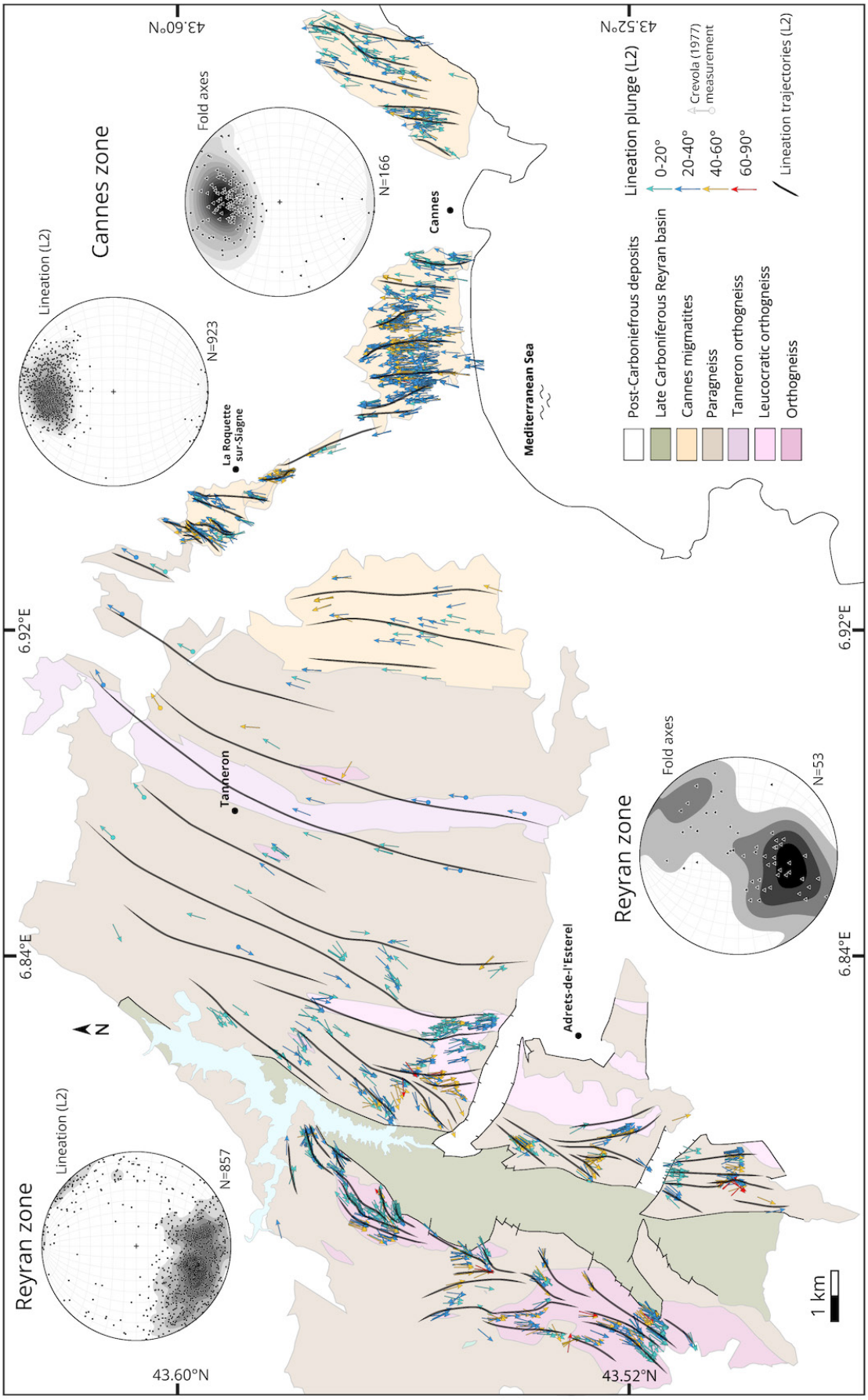

Figure 6 – Structural map of lineation trajectories (L2) reflecting the N-S subhorizontal flow of the crust. The curved trails highlight convergent and divergent patterns. Lower hemisphere stereograms of lineation and fold axes for the Reyran and Cannes zone are shown close to their respective areas.

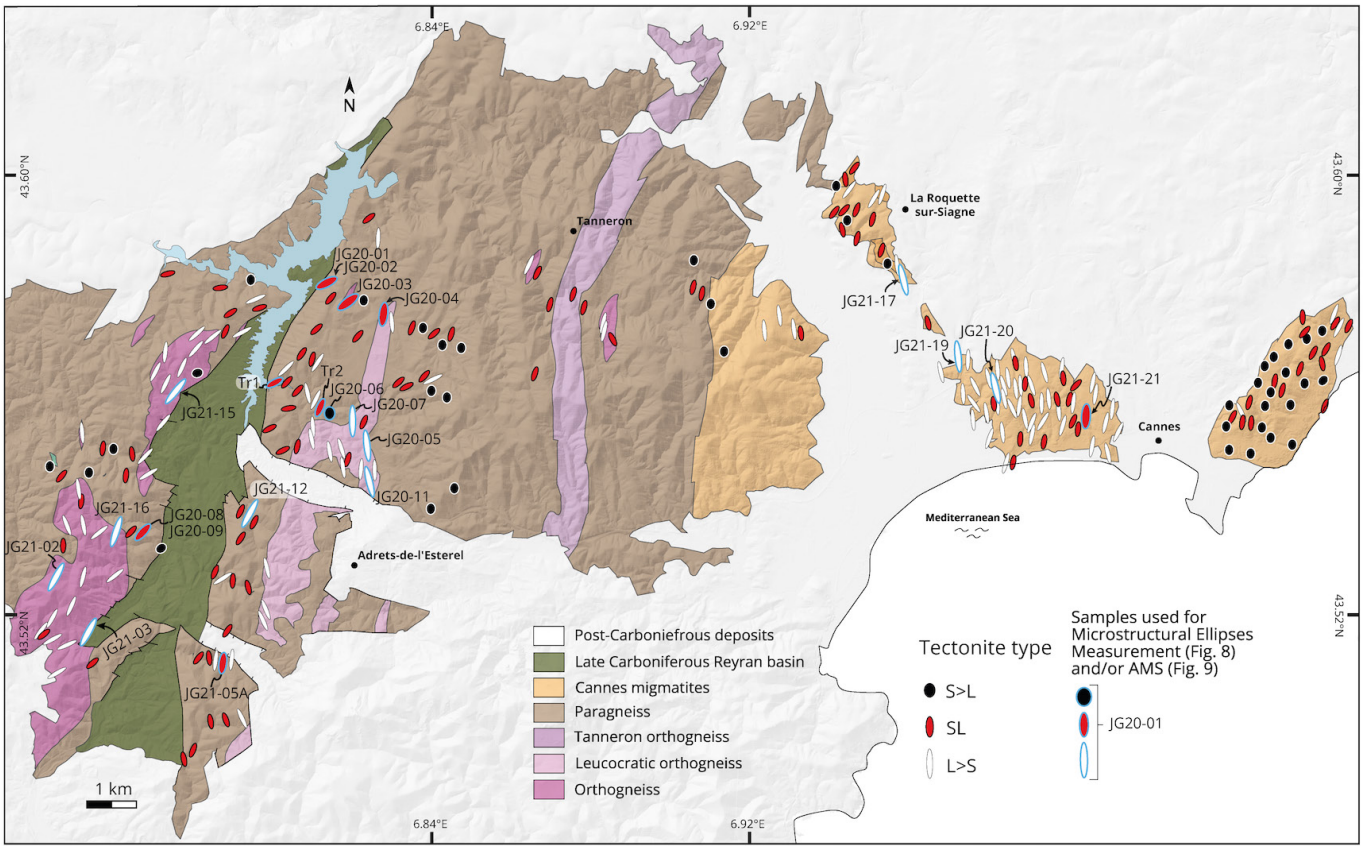

Figure 7 – Tectonite-type map based on field observations of S>L, S-L, and L>S tectonites classified according to three different symbologies of ellipses varying in colour and shape. Ellipsoids corresponding to samples used for Microstructural Ellipses Measurement and/or AMS are also indicated with a blue outline. A lithological influence is emphasised with orthogneiss showing mainly L>S tectonites whereas paragneiss are dominated by S-L tectonites. See also the contrasting tectonite type in the Cannes migmatite unit between the Croix des Gardes hill dominated by constrictional strain compared to the Super Cannes hill defining a mean flattening strain.

In order to confirm these macroscopic observations, finite strain ellipsoids were measured through microstructural analysis on 20 samples (Table 1, see Methodology section). Results for each sample recapitulate the apparent finite strain shapes determined from the field observations (Figure 7), with comparable structures being observed. The L-tectonite defines identical elongated quartzo-feldspathic or mica trails along the XZ plane while no clear orientation is visible in the YZ plane, which shows only rounded quartz/feldspars surrounded by micas (Figure 5E,F). Results are also compiled in a Flinn diagram which highlights a link between lithology and finite strain ellipsoid shape (Figure 8). Indeed, the paragneiss samples plot along the plane strain line (k=1) while most of the migmatitic orthogneisses and Cannes migmatites are gathered in the constriction field (k»1). Mylonite samples JG20-01/JG20-02/JG21-05A from the La Moure SZ plot close to the plane strain line supporting a simple shear flow for this strike slip SZ. Only one sample is located in the flattening field, demonstrating the monotony of the strong L>S and S-L tectonites which point to a rather homogeneous deformation pattern in the complete area.

4.4 Magnetic Fabric Parameters and Orientation (AMS)

AMS measurements were carried out on samples from three paragneiss sites, TR1, TR2, JG20-06 and two orthogneiss sites, JG20-05 and JG21-02 (Figure 9). Sites JG20-05/JG20-06/JG21-02 belong to the same sampling sites as the corresponding sample names used for microstructural ellipse measurements (Table 1). All analysed sites show a very good concordance between structural data measured in the field and the magnetic foliations and lineations (Figure 9). This suggests that magnetic minerals were deformed during the same tectonic event as the dominant quartzo-feldspathic phases and led us to analyse the potential contribution of other AMS parameters such as the degree of magnetic anisotropy (Pj) and shape parameter (T).

For sites TR1 (paragneiss) and JG20-05/JG21-02 (both orthogneiss), the bulk magnetic susceptibility (Km) varies between 50 and 270x10-6 [SI] (Figure 9), well within the <500x10-6 [SI] field that suggests the rock magnetic susceptibility is mainly carried by paramagnetic minerals (*Bouchez*, 2000; *Rochette*, 1987). Other observations (reflected-light microscopy, thermomagnetic curves and Km-Pj plot analyses (Figure 9)) are consistent with a

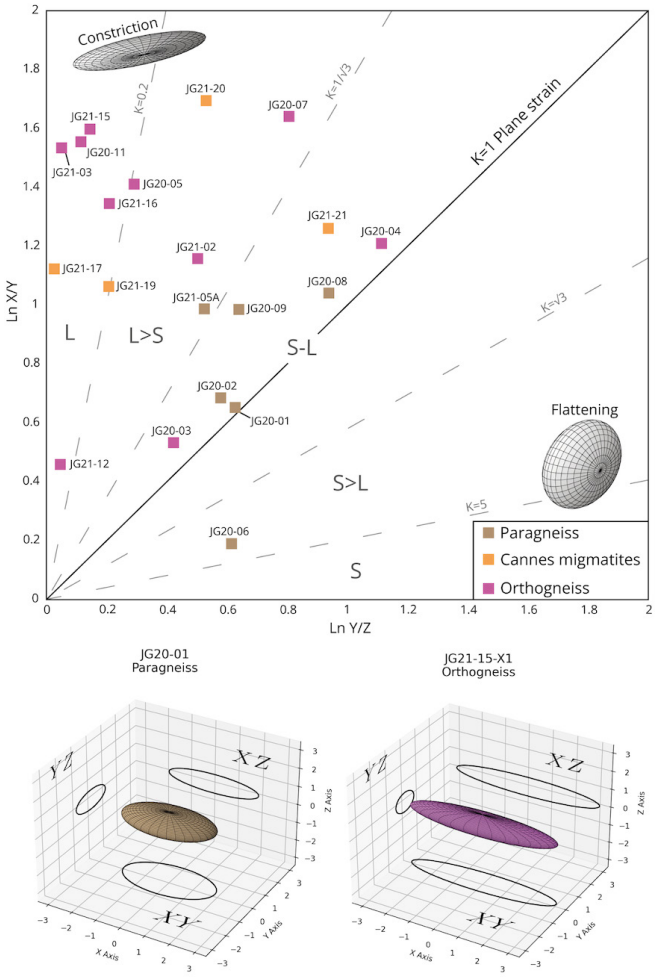

Figure 8 – Flinn diagram with plot of the 20 samples used for 3D finite strain ellipsoid calculation by microstructure measurement. Samples locations are shown in Figure 7 for reference. Two examples of 3D finite strain ellipsoids are shown for a paragneiss and orthogneiss sample in a 3D X-Y-Z axes diagram with projection of 2D ellipses on each corresponding section. The Flinn diagram reveals a lithological control on the shape of ellipsoids with the meta-sedimentary unit mainly distributed in the S-L domain whereas meta-igneous units are mostly confined to the L and L>S domains.

paramagnetic contribution to the rocks' magnetic susceptibility. Our petrological thin-sections show that biotite and muscovite are the dominant paramagnetic minerals and that biotite is always present in higher proportion than muscovite. Thus, biotite is expected to be the major contributor to the magnetic susceptibility in these sites. The Jelinek plot (Pj vs T) for these three sites gives values between -0.3 and 0.5, indicating that the T parameter plots mainly around 0 in the plane strain domain (Figure 9). This is in agreement with the observed SL tectonic style for TR1 (paragneiss) (Figure 7) but not for the L tectonites described for JG20-05 and JG21-02 (orthogneisses). Conversely, finite strain ellipsoid calculation has also confirmed the prolate strain shape of both sites (Figure 8).

Km values for sites TR2 and JG20-06 (paragneisses) are generally higher than other sites and lie in the approximate range of 300 - 3000x10-6 [SI]. TR2 shows a prominent linear correlation between Km and Pj (Figure 9) over a Km range of 350 to 2600x10-6 [SI]. Such a correlation, when associated with a mean magnetic susceptibility greater than 500x10-6 [SI], indicates a ferromagnetic carrier, in particular magnetite (*Henry et al.*, 2004; *Rochette*, 1987). Reflected-light microscopy and analyses of the thermomagnetic curves confirm the presence of magnetite. The Jelinek plot for site TR2 reveals a mean plane strain shape for the AMS ellipsoid (Figure 9), in agreement with observation of SL tectonites in the field (Figure 7). Bulk magnetic susceptibility (Km) values for site JG20-06 are divided into a tightly clustered group of 300 - 400x10-6 [SI] and a broader one of around 900 - 1300x10-6 [SI] with a slight linear correlation between Km and Pj (Figure 9). In view of the site's petrography, the low K group below 500x10-6 [SI] is more likely to be rich in biotite and the higher K group with the presence of ferromagnetic minerals. Each group gives a different ellipsoid shape in the Jelinek plot (Figure 9), with the biotite-related group plotting in the oblate domain and the ferromagnetic group values clustering in the oblate and plane strain domains. This pattern is repeated at site TR2, where the only two measurements with a bulk susceptibility lower than 500x10-6 [SI] in the Km-Pj plot also return the highest T values in the Pj vs T plot, where they approach the oblate shape domain. Both mineralogic groups in JG20-06 are broadly in agreement with the observed S>L tectonites in the field (Figure 7) and the oblate finite strain ellipsoid shape of JG20-06 plot in the Flinn diagram (Figure 8).

4.5 Deformation Temperature

Microstructural observations are used to constrain the relative deformation temperature across the area. Rocks of the eastern Tanneron Massif display a diversity of microstructures (Figure 10) indicative of their retrogression from high temperature suprasolidus fabrics down to subsolidus low temperature brittle-ductile fabrics.

High temperature conditions are inferred for the Cannes migmatite unit, which is mainly related to S2a foliation. These migmatites are composed of Qtz + Kfs + Pl + Bt + Ms ± Grt with no chlorite, unlike the other units. The texture is defined by homogeneous large quartz and feldspar grains (0.5-1.5 mm) aligned parallel to the L2 lineation in the foliation, which is typical of high-T regimes (Figure 10A) (*Gapais*, 1989). Some key microstructures indicative of melt-present deformation are recognisable, including interstitial phases with small dihedral angles, interstitial quartz melt infilling pore space, and elongated interstitial quartz and feldspar grains (*Lee et al.*, 2018; *Roberts and Tikoff*, 2021; *Stuart et al.*, 2018; *Zibra et al.*, 2012). In addition, dynamic recrystallisation of feldspar and quartz also indicates high-T deformation (*Roberts and Tikoff*, 2021).

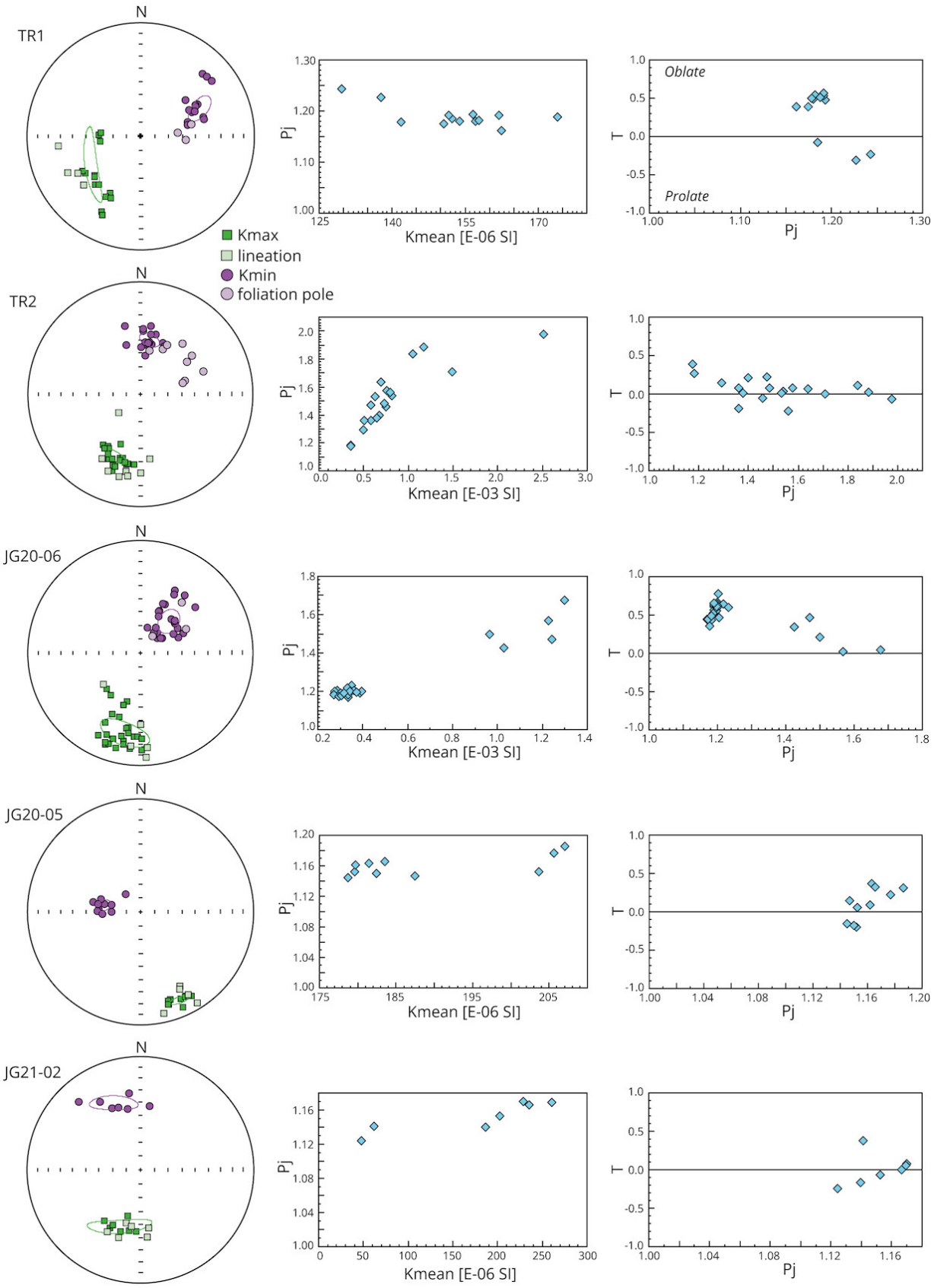

Figure 9 – AMS results with equal area, lower hemisphere projections of the principal magnetic susceptibility axes (Kmax and Kmin), Kmean-P plot and P-T plot for each sample. Geographically-referenced stereograms give foliation poles (S2) and lineations (L2) measured on each sample location compared to their AMS Kmax and Kmin values representing magnetic lineation and foliation, respectively. The confidence ellipses are computed from Jelinek's statistics (*Jelínek*, 1978). Kmean: (Kmax+Kint+Kmin)/3; P and T parameters are used to characterise the degree of magnetic anisotropy and the AMS ellipsoid shape, respectively. T ranges from -1 (prolate ellipsoid) to 1 (oblate ellipsoid) (*Jelínek*, 1978). Note variations in the order of magnitude of the abscissa scale. Sample locations are shown in Figure 7 for reference.

Figure 10 – Microphotographs showing the evolution from high suprasolidus down to low temperature deformation through microstructure evolution. This evolution follows a broad E-W cooling gradient. From A to D, note the intense grain size reduction due to increased recrystallisation and shear band development. **(A)** Cannes migmatite, sample JG21-20 located in a S2a domain, showing suprasolidus deformation textures (GPS coordinates: lat/lon = 43.5616/6.9808). Minerals are coarse, homogeneously aligned and stretched but without shear-bands, quartz is dynamically recrystallised through GBM textures, myrmekites and interstitial quartz melt infilling pore space are visible. Irregular, amoeboid quartz and feldspar boundaries are ubiquitous. **(B)** Migmatitic orthogneiss to the east of the La Moure SZ, sample JG20-07 located in a S2a domain, showing suprasolidus and subsolidus deformation textures (lat/lon = 43.5119/6.7877). In fact, in the upper part, the leucosome layer exhibits coarse grain size, amoeboid boundaries of GBM texture, myrmekites and interstitial quartz melt, which are characteristic of high temperature deformation. In the lower part, the grain size is smaller, discrete recrystallised shear bands are present, quartz is mostly recrystallised through SGR, indicating a colder deformation at subsolidus conditions. **(C)** Mylonite of migmatitic paragneiss from the outside of the La Moure SZ at the transition between S2a and S2b foliation domains, defined by middle to low temperature deformation textures (43.5579/6.8138). The main texture is a fine grain highly recrystallised matrix structured by dextral C and C' shear bands, with quartz SGR recrystallisation and muscovite fish. In the upper part, a preserved leucosome clast shows an early high temperature deformation texture with coarse grain size, quartz GBM texture and interstitial quartz melt. **(D)** Ultramylonite of migmatitic paragneiss from the core of the La Moure SZ (S2b foliation) at the contact with the Reyran Basin, sample JG20-01, showing a low temperature deformation texture (lat/lon = 43.5824/6.8167). The ultramylonite defines a completely recrystallised matrix of micrometric grain size (except muscovite fish) covered by a widespread anastomosed network of dextral S/C shear bands. These cold shear bands exhibit brittle-ductile deformation. Quartz is recrystallised through SGR and BLG textures. See section "Deformation temperature" for further detailed comments in the text.

Quartz exhibits typical grain boundary migration (GBM) with irregular and amoeboid boundaries (Figure 10A) that are considered to reflect temperatures exceeding 550°C (*Stipp et al.*, 2002). However, it is important to keep in mind that quartz dynamic recrystallisation is also dependent on strain rate.

Orthogneiss units, which are mainly related to S2a foliation, are also characterised by the presence of small dihedral angles of interstitial phases, interstitial quartz melt infilling pore space, and myrmekite around large K-feldspars, indicating the former presence of melt during the onset of deformation (*Lee et al.*, 2018; *Roberts and Tikoff*, 2021; *Stuart et al.*, 2018; *Zibra et al.*, 2012). In comparison to the Cannes migmatite, however, the orthogneisses have heterogeneous and smaller grain sizes (0.3-1mm) and discrete highly recrystallised shear bands that emphasise lower temperature conditions with subsolidus deformation (Figure 10B). Indeed, during the progressive evolution from suprasolidus to low grade (400-500°C) deformation, homogeneous penetrative foliation evolved to heterogeneous localised high strain shear bands showing a significant grain size reduction through dynamic recrystallisation (*Ebert et al.*, 2007; *Fossen and Cavalcante*, 2017; *Gapais*, 1989). Quartz dynamic recrystallisation is visible through high temperature GBM (Figure 10B) and also rare evidence for lower temperature subgrain rotation (SGR). Biotite and muscovite are recrystallised into smaller grains only within local shear bands. Some orthogneisses are composed of rare biotite transformed into chlorite.

Migmatitic paragneisses are composed predominantly of Qtz + Kfs + Bt + Ms with a variable proportion of chlorite, making up to 10% of the modal composition, and rare sillimanite. These paragneisses (which are mainly related to S2b foliation) have generally mylonitic textures with anastomosed shear bands around low strain domains or pervasive S/C structures, typical of amphibolite to greenschist facies deformation (*Fossen and Cavalcante*, 2017; *Gapais*, 1989). Grain size is significantly lower (0.2-0.5 mm) than in the Cannes migmatites or the orthogneiss and can be very heterogeneous, with large preserved grains from the early high temperature fabric (1-2 mm) surrounded by the main fine grain sheared matrix (0.1-0.2 mm). Biotite and muscovite are highly recrystallised into micrometric grains inside the mylonitic matrix while quartz is mainly recrystallised by SGR and shows preserved GBM textures or rare low temperature bulging (BLG). Biotite and chlorite occur in inter-boudin growth positions or inside shear bands, indicating syn-kinematic development. Hence, the widespread development of shear bands, grain size reduction, SGR/BLG textures and the significant chlorite amount point to medium to low temperature deformation in the presence of fluids from lower amphibolite to greenschist facies conditions. In addition, several preserved textures indicate an earlier high temperature deformation: small dihedral angles of interstitial phases (*Stuart et al.*, 2018), quartz dynamic recrystallisation through GBM, ductilely deformed feldspar, and the presence of sillimanite in the melanosome. Inside the La Moure SZ, an increasing strain gradient accompanied by a decreasing deformation temperature (Figure 10) closer to the Reyran Basin border may be inferred from microstructure analysis. Migmatitic paragneisses close to the Reyran Basin border show a higher grain size reduction and increased prevalence of brittle-ductile shear band development than elsewhere, and are characterised by SGR and few BLG quartz recrystallisation whilst eastern migmatitic paragneisses of the shear zone preserve more GBM textures (Figure 10). These low grade ultramylonites, derived from migmatitic paragneisses, are mostly localised on the border of the Reyran Basin but the strong spatial variation of their chlorite proportion, and the associated intense weathering of the basement, leave it impossible to map them as a separate unit. Consequently, we avoid using the term.

Deformation temperature, inferred from the study of microstructures, emphasises an east-west syndeformational cooling gradient. Indeed, the Cannes migmatites are described by high temperature fabrics with a main suprasolidus deformation while orthogneisses and paragneisses show microstructures indicative of subsolidus deformation until low-T conditions near the brittle-ductile transition along the Reyran Basin border. Interestingly, all units are characterised by the presence of preserved microstructures designating suprasolidus deformation. In detail, microstructures also reveal contrasting deformation temperatures between meta-igneous and meta-sedimentary rocks with the Cannes migmatites and migmatitic orthogneiss being deformed at suprasolidus and/or high temperature subsolidus conditions while migmatitic paragneiss show rare early high temperature deformation textures subsequently overprinted by dominant medium to low-temperature fabrics. Because S2a foliations are more developed in the Cannes migmatite and orthogneiss unit and S2b foliation in the paragneiss unit, this means that deformation temperature was higher for the S2a fabric than S2b fabric.

5 Discussion

5.1 Origin of the Cryptic Cannes Structure

The Cannes migmatites exhibit a complex structure, highlighted by distinct differences between the Croix des Gardes and Super-Cannes hills. In the Croix des Gardes area, constrictional flow with strongly deformed L>S tectonites is prevalent, and defines the rock architecture (Figures 5 and 7). In contrast, the Super-Cannes sector displays mainly flattening

strain on slightly deformed sub-horizontal foliations (Figures 4 and 7). The Croix des Gardes hill is defined by monotonous E-W striking S2a, locally reworked by N-S S2b, while the Super-Cannes hill presents a more chaotic pattern of S2a (Figure 3). The latter exhibits a folded structure with various orientations, emphasised by foliation triple points and a sub-dome structure in the western part. Despite these differences, both areas share a common lineation pattern, with stretching lineations (L2) consistently plunging between N000-N020°, indicating the need for their integration within the same global framework.

The preserved migmatitic nature of the Cannes migmatite unit (Figure 2E, F), observable through its suprasolidus deformation structures, suggests two possible models to explain the observed architecture: a tectonic dominated model and a buoyancy-isostasy dominated model (*Kruckenberg et al.*, 2011). The tectonic dominated model implies that constrictional and flattening fabrics from each sector must be kinematically consistent in the same strain regime, which appears conflicting. Additionally, the sub-dome concentric foliation orientations and the deflection of foliations around triple points are challenging to reconcile with a common kinematic regime. Conversely, buoyancy-isostasy driven flow, as documented for diapirism (*Dixon*, 1975; *Cruden*, 1990), can explain the highly variable orientations of flattening fabrics. Diapirism also predicts the coexistence of flattening and constrictional fabrics, with constriction expected in the core of a rising diapir and flattening around the outside and the top (*Cruden*, 1988, 1990; *Sullivan*, 2013; *Talbot and Jackson*, 1987).

In hot orogens with buoyant lithosphere, field-based structural studies have demonstrated that flat fabrics in lower crustal levels may consist of vertically shortened and horizontally sheared roofs of domes (*Dirks et al.*, 1997; *Gapais et al.*, 2005, 2008; *Gébelin et al.*, 2007). In this scenario, the Croix des Gardes hill could represent the inclined diapir centre, and Super-Cannes the flattened outside. Alternatively, a third option to explain these contrasting structures could involve variations in the exposed structural level, with Croix des Gardes as a diapir core characterised by constriction and Super-Cannes as a diapir roof characterised by flattening. In this model, the migmatite dome is divided into several N-S directed inclined subdomes with axes following the stretching lineation, where each hill represents a different diapir.

Gravity-driven flow is a plausible process to account for some of the structural features within the Cannes migmatite unit. However, the continuous lineation field (L2) between both areas and the presence of S2b vertical foliation zones cannot be fully explained by gravity-dominated forces alone. Foliations wrapping around the average lineation direction, a common tectonic feature of syn-tectonic domes (*Darrozes et al.*, 1994; *Djouadi et al.*, 1997; *Nédélec and Bouchez*, 2015), are also recognised in the field (Figure 5A-B) and documented in this study (Super-Cannes hill stereograms: Figures 3 and 6). These observations suggest that flow within the migmatitic unit was controlled by a combination of independent internal gravity forces and a strong oblique tectonic framework. Elongated migmatitic domes parallel to the stretching direction can form in zones of local horizontal flow within a transtensive regime (*Denèle et al.*, 2017; *Le Pourhiet et al.*, 2012; *Rey et al.*, 2017).

The Super Cannes hill, representing a tectonically preserved area, is dominated by high-temperature structures related to internal buoyancy-driven flow rather than tectonic forces. This is supported by its specific eastern location, representing the most internal part of the unit, combined with the greater presence of nebulitic facies and lower strain migmatites (Figure 2E,F). In contrast, the presence of strongly stretched L-tectonites and S2b vertical foliations at the Croix des Gardes and Roquette hills indicates an increasing influence of tectonic forces when moving westward in the massif.

5.2 Lithological Control on Finite Strain Ellipsoid Measurements

Finite strain analyses reveal contrasting ellipsoid shapes between different lithologies. Paragneiss lithology is mainly associated with S-L tectonite on the map scale (Figure 7) and plots along the plane strain line (Figure 8), while Cannes migmatites and orthogneiss units are characterised by numerous L>S tectonites (Figure 7) and fall within the constrictional field of the Flinn diagram (Figure 8). This contrast is evident in the field, where transitions between these lithologies often exhibit a sharp change marked by the appearance of strong stretching lineations (L2) and L>S tectonites. Phyllosilicate-rich paragneiss units, derived from meta-sedimentary series, are considered rheologically weaker than orthogneiss and Cannes migmatites. This suggests that heterogeneous and weaker lithologies display more evidence for plane strain deformation, while homogeneous and stronger lithologies are characterised by constrictional strain deformation.

Rheologically driven strain path partitioning, with the concentration of L-type tectonite in stronger homogeneous units, has been described in previous studies (*Fletcher and Bartley*, 1994; *Sullivan*, 2006, 2008, 2013) and partitioning of non-coaxial deformation into rheologically weak domains, such as schist units, is predicted by many field observations, theoretical studies and numerical simulations (*Goodwin and Tikoff*, 2002; *Goodwin and Williams*, 1996; *Jiang*, 1994a,b; *Lister and Williams*, 1983; *Sullivan*, 2008, 2013). Thus, we propose two potential scenarios to explain this rheology-dependent finite strain shape variation: strain path partitioning with each

lithology accommodating a single deformation phase differently, or each lithology recording different deformation phases. The consistent structural lineation (L2) field transcending all lithologies and widespread folding of most units with axes parallel to this stretching lineation (L2) support strain partitioning during a single deformation phase. However, several factors suggest that the observed rheologically driven finite strain shape contrast is caused by differential recording of two deformation phases during a progressive deformation event.

First, L>S tectonite types inside meta-igneous units are mostly associated with the low-strain and high-T S2a foliation, which is primarily confined to these lithologies, while high-strain medium to low-T S2b foliations are mainly visible in the paragneiss unit defined by S-L tectonite. Second, S2a foliations are transposed and overprinted by S2b foliations, highlighting a deformation chronology (Figure 3). Finally, microstructural analyses reveal that deformation in meta-igneous units occurred at higher temperatures than in the meta-sediment units (Figure 10). Thus, we suggest that the constrictional flow and associated S2a foliations were formed during a first deformation phase, subsequently overprinted by a second phase represented by S2b foliations.

Contrary to expectations, meta-sedimentary units, which are mainly deformed by high strain S2b foliation and associated SZ, do not plot in higher deformation domains than meta-igneous units in the Flinn diagram, and the opposite is even observed (Figure 8). In fact, the leucosomes and/or quartz layers chosen as reference material for ellipse calculations were excessively sheared until recrystallisation into smaller lenses and clasts during the second phase, erasing their stretched shape from the first phase. High strain deformation mechanisms at middle to low temperatures tend to reduce grain size and spread-out former fabrics (*Ebert et al.*, 2007; *Fossen and Cavalcante*, 2017; *Gapais*, 1989), which could lead to minimised finite strain intensity with the ellipse method used in this study.

The magnetic foliation and lineation of each site are in the same range as structural measurements in the field. The orientation of the principal axes (Kmax, Kint, Kmin) from AMS measurements could therefore provide a valuable complement to field measurements. However, the use of AMS to quantify finite strain and study the shape of the finite strain ellipsoid remains limited, as pointed out by various authors (e.g., *Borradaile and Henry*, 1997; *Borradaile and Jackson*, 2010). AMS combines contributions from all magnetic minerals (diamagnetic, paramagnetic and ferromagnetic), which could develop distinct magnetic fabrics.

The AMS ellipsoid shapes for sites of low magnetic susceptibility values with a magnetic mineralogy dominated by paramagnetic minerals, in particular biotite, give opposite results to observed and measured finite strain ellipsoids for strong L-tectonites (JG20-05 and JG21-02, Figure 9). The shape anisotropy of micas is known to generate generally oblate AMS ellipsoids (*Rochette et al.*, 1992), which is well illustrated by sites TR2 and JG20-06 in which measurements attributed to paramagnetic biotite give more oblate values than those from ferromagnetic minerals in the same rock (Figure 9). The observed poor correlation between the shape of AMS and finite strain ellipsoids for constrictional strain in this study was previously reported in published studies where oblate AMS ellipsoids were obtained from L>S tectonite in gneiss with a magnetic susceptibility controlled by micas (*Das et al.*, 2021; *Skyttä et al.*, 2010).

Conversely, AMS sites richer in ferromagnetic minerals (TR2 and JG20-06) provide a good correlation with observed and measured finite strain ellipsoids (Figure 9). This good agreement could be due to the presence of magnetite, which is characterised by a grain-shape alignment anisotropy (*Borradaile and Henry*, 1997; *Borradaile and Jackson*, 2010; *Ferré et al.*, 2014). The determination of the sub-fabric carried by the ferromagnetic minerals by using magnetic remanence anisotropy techniques, for example (*Hrouda*, 2002; *Jackson*, 1991), could better constrain and use the AMS measurements.

5.3 Transpression vs Transtension?

The internal part of the Maures-Tanneron Massif aligns with an oblique tectonic framework, particularly due to the vertical shear zone's strike-slip component associated with shallowly plunging lineation, which trends at a low angle to the shear's strike. Fold axes parallel to the regional lineation (L2) are another common feature of oblique tectonic systems (*Fossen et al.*, 1994, 2013). A transpressional tectonic setting was previously proposed by *Rolland et al.* (2009), based on the observation of a dome structure around the Rouet granitic intrusion and N-S kilometer-scale folds defining the structure of the Tanneron Massif, following the previous interpretation made by *Crevola* (1977). This transpression context is inferred for the entire Maures-Tanneron Massif. However, in the eastern Tanneron, representing the more internal part of the massif, our results point to a transtensional event. The kilometer-scale folds described by *Crevola* (1977) (and after *Rolland et al.*, 2009) are not observed, and we identify two sets of planar fabric with a main S2b vertical foliation. Moreover, numerous folds of different geometries are visible in the field, but they do not necessarily indicate a convergence context, as folds can form readily during transtension (*Fossen et al.*, 2013), or progressive constrictional strain as experimentally demonstrated by *Ghosh et al.* (1995). Analytical models (*Fossen and Tikoff*, 1993; *Fossen et al.*, 1994, 2013) demonstrate that fold axes evolve from vertical to horizontal plunge during transtension while the opposite is predicted for transpression, and fold axis direction tends to rotate

parallel to the SZ boundary for transpression while retaining an angle of 10-15° even for simple shear dominated transtension (*Fossen et al.*, 2013). Here, fold axes have a mean 10-30° plunge and their orientations follow the lineation (L2), which mainly strikes at an angle of 20-30° to the La Moure SZ reference. Therefore, fold axis orientations and plunges match characteristics of transtensional folds more than transpressional folds. Additionally, stretching lineations parallel to fold axes are seen as a signature of transtension at the middle-lower crustal level (*Fossen et al.*, 2013) and transtensional folds are often associated with constrictional strain and large magnitude stretching, which align with our data.

Various analytical models have studied oblique tectonics through different combinations of pure and simple shear applied to a deforming volume stuck between rigid boundaries (*Dewey et al.*, 1998; *Fossen and Tikoff*, 1993, 1998; *Jones et al.*, 2004; *Sanderson and Marchini*, 1984). In terms of strain, all models show that transpression develops flattening strain, whereas transtension favours constrictional strain. In the Tanneron Massif, finite strain shape analysis supports widespread gently dipping constrictional flow, indicating the importance of L and L>S tectonites (Figures 7 and 8). L or L>S tectonites are predicted within the Flinn diagram as a common feature for transtension, with associated well-developed lineations remaining oblique to the shear direction (*Fossen and Cavalcante*, 2017; *Sanderson and Marchini*, 1984). This is in agreement with the lineation field (L2) of the area remaining mainly oblique to the shear direction (20-30°) (Figure 6). Various analytical graphs developed in *Fossen et al.* (2013) could be used, combining ellipsoid principal strain axes or fold tightness data and/or angles with the SZ, to distinguish between transpression and transtension regimes and to obtain theoretical dynamic vorticity Wk values for the subsimple shear deformation. In our data, the length of minimum horizontal principal strain axis (Z or Y) ranges between 0.67 and 0.32 with a mean of 0.52 and the length of maximal horizontal principal strain axis (X) varies between 1.38 and 3.90 with an average of 2.54. Folds in the area are mostly close to tight, matching the corresponding range of Z axis lengths as proposed by *Fossen et al.* (2013). Assuming an average angle of 20-30° between the lineation (L2) and SZ, graphs comparing this angle with length of principal strain axis (X or Z) mainly give values approaching the simple shear curve, which mostly plot as simple shear dominated transtension (*Fossen et al.*, 2013, Figures 4 and 7). Wk values vary between 0.8 and 1, highlighting the dominance of simple shear flow. The X axis vs Z axis plot also shows most data corresponding to simple shear dominated transtension with vorticity ranging between 0.8 and 1 and a Wk value of 0.95 by considering the mean values for length of the X and Z axes (*Fossen et al.*, 2013, Figure 8). These high vorticity numbers are in agreement with the predicted rotation of folds, requiring a minimum Wk of 0.7 to obtain fold axes with angles of 20-30° relative to the SZ, as observed in the area (*Fossen et al.*, 2013, Figure 5). Theoretical gamma (γ) values of the shear strain are also provided in these graphs and vary approximately between 1.5 and 2.5, which emphasises the high strain deformation in these late transtensional regimes.

The combination of constrictional strain and domes representing the pure shear component and S-L tectonites through strike-slip SZ representing the simple shear suggests a general transtensional tectonic framework in the Tanneron Massif. This regime manifests during the late-stage evolution of the massif between 325-295 Ma, associated with an oblique collapse of a hot crust. In the internal part of the Maures Massif, a strong longitudinal horizontal crustal flow was recently highlighted by the predominance of subhorizontal stretching lineations, striking continuously N-S through the migmatitic basement (*Bolle et al.*, 2023). These authors suggest that this subhorizontal extension associated with strike slip SZ induced thinning of the continental crust associated with partial melting, granitic intrusions and exhumation of the lower continental crust during the latest event of the belt (325-298 Ma). In addition, late dextral shear-zones developed from near-solidus amphibolite metamorphic facies down to brittle-ductile conditions are described in the MTM (*Simonetti et al.*, 2020a) and Corsica-Sardinia block (*Frassi et al.*, 2009; *Giacomini et al.*, 2008), which agree with our description of the second phase and the development of the La Moure SZ.

A key element is the opening of the Carboniferous Reyran Basin, which strikes parallel to the surrounding La Moure SZ (N10-20) (Figure 3). This pull-apart basin is thought to have opened around 310-300 Ma (*Toutin-Morin et al.*, 1994), roughly synchronous with the end of the basement oblique tectonic event. The nearby La Moure SZ and the basin's particular shape, which might be described as four former NE-SW en-echelon sub-basins (Figure 1), support the opening within an oblique tectonic regime. Moreover, Carboniferous sediments are strongly folded in specific sectors, suggesting potential syn-sedimentary deformation (Maillet, 2021). In this context, the opening of this type of basin is more likely to occur within a transtensional regime because the stretching component of transtension contributes to thinning the crust, contrary to the vertical flattening strain developed through transpression. In the Variscan belt, the opening of a pull-apart basin during a dextral transtensional regime between 315-300 Ma was also described in the Montagne Noire (*Chardon et al.*, 2020; *Franke et al.*, 2011; *Rey et al.*, 2017).

The proposed tectonic evolution defining a late-stage oblique regime at the end of the Variscan cycle is in good agreement with previous studies

in the MECS microplate. However, most of these studies have described late-stage deformation in a transpressional regime (MTM: *Rolland et al.*, 2009; *Simonetti et al.*, 2020a; Sardinia: *Carosi et al.*, 2012, 2020; *Frassi et al.*, 2009), while references to transtensional regimes, as we propose here for the Tanneron Massif, are scarce and brief (MTM: *Buscail*, 2000; Corsica: *Thevoux-Chabuel et al.*, 1995). This can either be because the proportion of transtensional kinematics during the late-stage event has been underestimated or overlooked, or because both oblique regimes (transpression and transtension) may have been active simultaneously but partitioned in space. Based on our observations and results we believe that transtensional deformation could better describe the late oblique event in the MECS, in particular due to the ubiquitous horizontal stretching flow observed in the whole MTM, general thinning and exhumation of the orogenic crust and the opening of Carboniferous basins. More extensive structural analyses, as we present here, are needed in other internal parts of the MECS to unravel a full picture of the late-orogenic kinematics of this Variscan segment. Considering the rest of the Southern European Variscan belt, our results are in line with numerous other studies describing also an oblique deformation regime in various areas of the belt during the late-orogenic event supporting the waning of the Variscan cycle. There too, transpressional regimes (Iberian Massif: *Fernández and Pereira*, 2017; Pelvoux Massif: *Fréville et al.*, 2022; French Massif Central: *Gébelin et al.*, 2007, 2009; Belledone Massif: *Jacob et al.*, 2021; Montagne Noire: *Rabin et al.*, 2015; Argentera Massif: *Simonetti et al.*, 2018; Aiguilles-Rouges Massif: *Simonetti et al.*, 2020b; *Vanardois et al.*, 2022; Agly Massif: *Vanardois et al.*, 2020) have been advocated over transtensional ones (Montagne Noire: *Rey et al.*, 2017). It should however be noted that none of these other massifs, except for the Montagne Noire, displays such a strong subhorizontal constrictional flow as we describe here. Our results suggest that part of the Variscan belt would perhaps deserve to be re-examined through the transtensional model, as it seems more suitable to explain the observed widespread Carboniferous basins' opening and the overall thinning of the belt driving its orogenic collapse.

5.4 Progressive Deformation and Strain Partitioning During Exhumation

In our structural analysis, we identified two distinct strain patterns and divided planar fabrics into two sets: an E-W flat lying S2a foliation and a N-S vertical S2b foliation (Figure 3). The S2a foliation is primarily observed in the Cannes migmatites and orthogneiss unit, while the S2b foliation is more prevalent in the paragneiss unit. Finite strain shape ellipsoids are also grouped according to lithological units, with prolate strain associated with ortho-derived units and plane strain with paragneiss (Figures 7 and 8). A constrictional strain regime characterised by ubiquitous stretching lineations (L2) and L>S type tectonites is associated with S2a foliations in meta-igneous units. In contrast, a plane strain regime defined by S-L tectonites is supported by S2b foliations in the mica-rich paragneiss. S2a foliations are locally transposed by S2b foliations (Figure 3), and microstructure analyses indicate higher deformation temperatures in ortho-derived units than in paragneiss (Figure 10). These observations suggest a two-phase progressive deformation event during the retrograde metamorphic evolution, associated with the collapse of the belt.

We propose a two-phase model in which two intermediate deformation phases represent increments of a progressive deformation during the evolution of a single transtensionnal event. The first phase involves the deformation at mid-crustal depth of all lithological units by a gently-dipping constrictional strain, creating L>S tectonites and the S2a foliation. This phase represents the sub-horizontal flow of the migmatitic crust at high temperatures. Some parts of the crust with a higher degree of anatexis are partially preserved from tectonic forces and experience doming and internal buoyancy-driven flow, as seen in the Super-Cannes hill (see section 5.2). The second phase is characterised by a plane strain flow that develops the S2b foliation and associated strike-slip shear zones. Deformation is partitioned into the paragneiss unit, enveloping ortho-derived lithologies that preserve their stretched shape from the first phase and are generally not, or minorly, overprinted. At the map scale, orthogneiss in the Reyran zone can be seen as finite strain markers representing prolate cigar-like bodies, shaped by the interaction of their internal stretching lineation orientation and plunge with the topography. The plane strain deformation starts at high temperatures following the first phase, as observed in the western parts of the Cannes migmatites, but intensifies at lower temperatures in the paragneiss unit during the subsequent cooling of the hot crust. A strain gradient from the Cannes migmatites to the La Moure SZ is accompanied by a deformation-related temperature gradient from near solidus to chlorite isograd (Figure 10). This indicates that during the second phase, deformation begins at high temperatures across the entire area before progressively localising westward at lower temperatures, following strain softening until the onset of the La Moure SZ. The high strain SZ remains active until low temperatures are achieved, leading to cataclastic flow and the opening of the Reyran pull-apart basin in which L-tectonite blocks are found within the conglomerates.

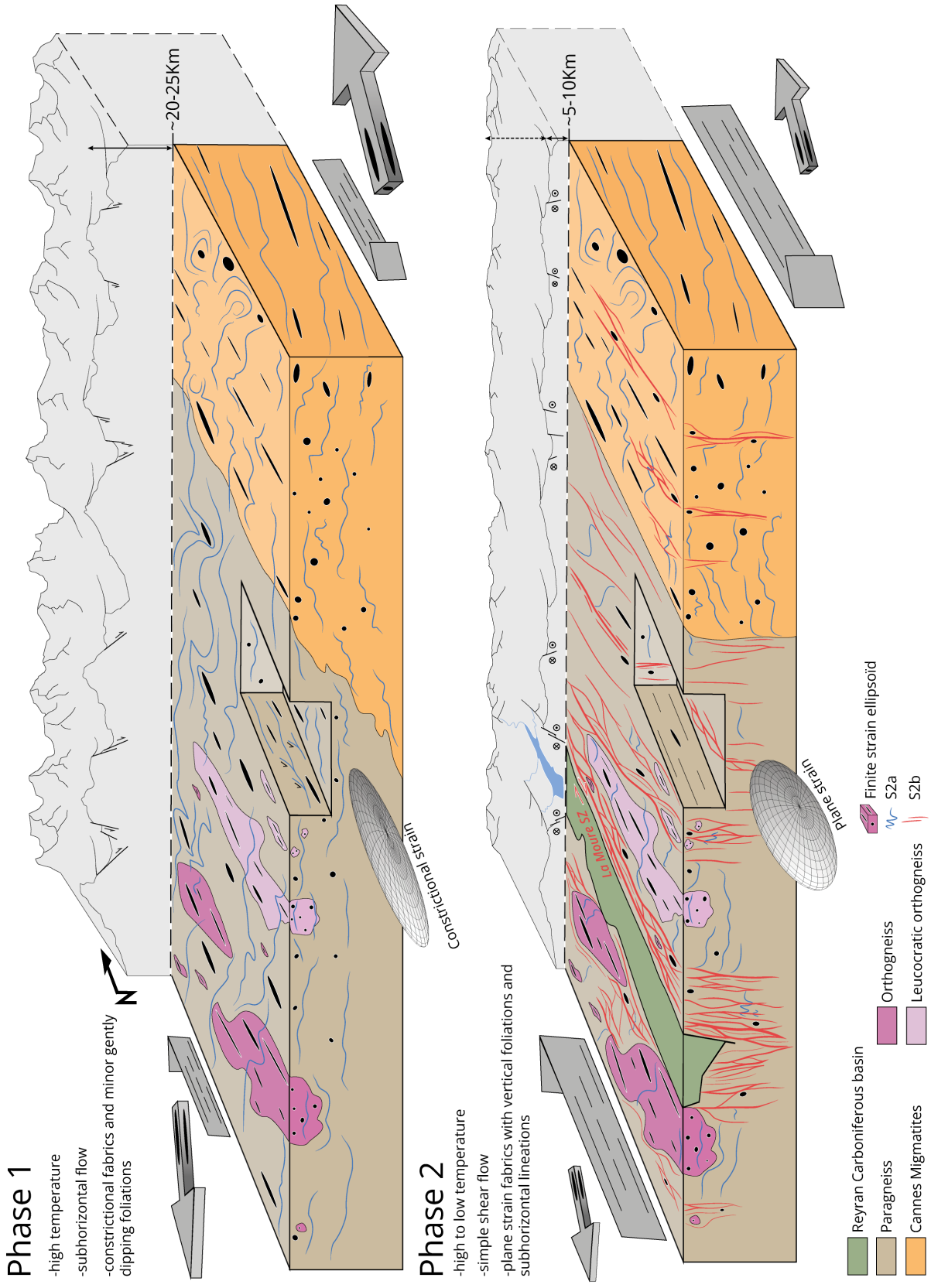

Figure 11 – Synthetic 3D diagram showing the tectonic evolution of the transtensional regime (~325-295 Ma) from phase 1 to phase 2. Strain patterns evolve from an initial horizontal S2a foliation associated with gently dipping N-S pure shear constrictional flow, to a second vertical S2b foliation combined with simple shear plane strain flow represented by the development of an anastomosed network of local shear zones and the major La Moure SZ. During the second phase, rheologically driven strain partitioning can be seen in the preferential localisation of the plane strain flow in the paragneiss unit, enveloping orthogneiss bodies that preserved their stretched shape from the first phase. The second phase also highlights a localisation and migration of deformation from east to west, illustrated by the increasing development of the S2b foliation, which is confined to local corridors in the Cannes area and widens westwards in the Reyran area until it intensifies around the Reyran Basin with the La Moure SZ.

These two deformation phases highlight changes in the global transtensional regime, which could be represented by a combination of strike-slip and coaxial perpendicular extension (Figure 11). During the first phase, the pure shear orthogonal component (corresponding to prolate fabrics) dominates over the simple shear component. In contrast, the second phase is characterised by a simple shear-dominated flow represented by plane strain fabrics and vertical SZ. This progressive change of the transtensional regime could reflect an evolution of the transport direction. The switch from a first S2a foliation overprinted by the subsequent S2b foliation would represent a rotation of the extension direction, becoming more parallel to the transcurrent shear direction. In fact, when the angle between the transport direction and the transtension zone boundary is greater than 20°, the coaxial component associated with vertical shortening and horizontal foliation dominates, while for angles less than 20° the transtension is dominated by the non-coaxial component, horizontal shortening and vertical foliation (*Dewey*, 2002; *Teyssier and Tikoff*, 1999). A second option is to consider the rheological influence on strain evolution due to cooling and preferential hydration of the crust during its progressive exhumation. In this hypothesis, the first constriction (pure shear) dominated transtension would only be possible with a hot crust that needs to be sufficiently weak to flow horizontally. Then, the progressive cooling and crystallisation of the crust will inhibit constrictional flow and promote strain localisation in the weaker paragneiss, leading to a simple shear dominated transtension.

Deformation localisation in the paragneiss unit during the second phase, rather than in meta-igneous rocks, exemplifies rheologically driven strain partitioning (*Carreras et al.*, 2013; *Fossen et al.*, 2019). After the crystallisation of anatectic melt, weak mineralogical phases other than melt control the rheology of metamorphic rocks (*Diener and Å*, 2014; *Hunter et al.*, 2016; *Vanardois*, 2021). The Tanneron Massif's progressive exhumation leads to the crystallisation of meta-igneous rocks, which gradually strengthen these units, acting as stronger homogeneous bodies within the weaker heterogeneous paragneiss unit. The high rheological contrast of meta-igneous rocks may deflect strain paths and localise them in surrounding weaker units (*Gremmel et al.*, 2023). The paragneiss unit also contains a higher mica modal proportion than meta-igneous rocks, which is the weakest mineralogical phase and would control strain localisation at subsolidus conditions (*Handy*, 1994; *Hunter et al.*, 2016; *Montési*, 2013). Typically, micaceous rocks deform more easily than quartzo-feldspathic rocks (*Fossen et al.*, 2019). Strain localisation is also expected within rocks with layered fabrics (*Handy*, 1990; *Hunter et al.*, 2016; *Montési*, 2013), especially with micaceous fabrics (*Shea and Kronenberg*, 1993; *Wintsch et al.*, 1995), as seen in the meta-sediment unit compared to the meta-igneous units. This concept is sometimes referred to as "geometric softening" (*Fossen and Cavalcante*, 2017; *Ji et al.*, 2004; *Passchier and Trouw*, 2005; *Rutter et al.*, 2001). Consequently, the plane strain deformation phase in the study area progressively localises in the paragneiss unit during retrogression from sub-solidus down to low metamorphic grade due to strain hardening of crystallising meta-igneous units, creating a strong rheological and geometrical contrast. This strain partitioning arises during a general transtensive regime associated with the progressive oblique thinning of this collapsing hot orogen.

6 Conclusion

The preserved migmatitic basement of the eastern Tanneron Massif lies in a crucial position between coeval deformation of partially molten rocks and opening of a pull apart basin, providing a unique opportunity to study the progressive collapse of a hot orogen during an oblique tectonic event. The study of this late Variscan oblique regime reveals transtensional kinematics divided into two intermediate deformation phases. The first phase involves a subhorizontal flow with dominant constrictional fabrics (L>S tectonites) and minor gently dipping foliations at high temperature conditions. Then, a simple shear flow characterised by plane strain fabrics (S-L tectonites) with vertical foliations and subhorizontal lineations was active from high to low temperature conditions. Vertical foliations are distributed in a widespread network of anastomosed shear zones with the dominant dextral kinematics represented by the major La Moure SZ, which was active until the opening of the Carboniferous Reyran Basin. The transition between the two phases is not interrupted; deformation was progressive within the same general transtensional regime and the two phases may have been briefly synchronous.

The field-based model presented in this study highlights important aspects of 3D strain distribution in ductile oblique regimes and can contribute to better understanding these complex structural frameworks and related strain patterns. These findings will be useful as a model for comparison with other suspected transtensional systems in hot orogens, and particularly for the numerous Variscan massifs described by late oblique deformation synchronous with the opening of Carboniferous basins. In addition, the progressive strain evolution from suprasolidus deformation down to greenschist facies followed by brittle deformation with the opening of a pull apart basin shows how transtensional regimes can efficiently and quickly lead to the exhumation of an unstable thickened crust.

The present study further illustrates how

multi-method structural analysis, here through precise digital mapping coupled with complementary microstructural observations and finite strain quantification, are necessary to unravel and classify different strain patterns and their evolution in complex structural domains such as oblique tectonic regimes.

Acknowledgements

Jean-Marc Lardeaux and Pierre Trap are gratefully acknowledged for stimulating discussions. We also thank Pierre Trap for his generous support of a Keyence microscope providing high-resolution microphotography. We are also grateful to Aude Gebelin and an anonymous reviewer for their very constructive comments during the review process. We are very grateful to the two editors Graeme Eagles and Kim Welford for their helpful comments and thorough editorial work on the revised version of the manuscript, and to Mohamed Gouiza for his meticulous and conscientious work on proof editing. This work was supported by the Tellus Program of CNRS-INSU, the CSI program of Université Côte d'Azur, and Géoazur Laboratory.

Author contributions

Field work, conceptualisation, data analysis, creation of figures, visualization and writing were mainly conducted by **JG** in close cooperation with **GD**. Field work has also been carried out with **MC** and **JB**. AMS data analysis was performed by **JG** and **JB**. Project funding by **GD**.

Data availability

The original structural data from field measurements (metamorphic foliations, mineral and stretching lineations, folds (axial planes and fold axes), and tectonite-style) are available at a public data repository. Data were acquired in the field using a digital tablet (iPad mini) and FieldMove software.

Competing interests

The authors declare no competing interests.

Peer review

This publication was peer-reviewed by Aude Gébelin and an anonymous reviewer. The full peer-review report can be found here: tektonika.online/index.php/home/article/view/69/106

Copyright notice

References

Alvarado, D., C. DeMets, B. Tikoff, D. Hernández, T. F. Wawrzyniec, C. Pullinger, G. Mattioli, H. L. Turner, M. Rodriguez, and F. Correa-Mora (2011), Forearc Motion and Deformation between El Salvador and Nicaragua: GPS, Seismic, Structural, and Paleomagnetic Observations, *Lithosphere*, *3*(1), 3–21, doi: 10.1130/L108.1.

Archanjo, C. J., R. I. F. Trindade, J. L. Bouchez, and M. Ernesto (2002), Granite fabrics and regional-scale strain partitioning in the Seridó belt (Borborema Province, NE Brazil): GRANITE FABRICS IN THE SERIDÓ BELT, *Tectonics*, *21*(1), 3–1–3–14, doi: 10.1029/2000tc001269.

Asti, R., N. Saspiturry, and P. Angrand (2022), The Mesozoic Iberia-Eurasia diffuse plate boundary: A wide domain of distributed transtensional deformation progressively focusing along the North Pyrenean Zone, *Earth-science reviews*, *230*(104040), 104,040, doi: 10.1016/j.earscirev.2022.104040.

Bascou, J., B. Henry, R.-P. Ménot, M. Funaki, and G. Barruol (2013), Contribution of AMS measurements in understanding the migmatitic terrains of Pointe Géologie, Terre Adélie (East-Antarctica), *Tectonophysics*, *603*, 123–135, doi: 10.1016/j.tecto.2013.05.021.

Bellot, J.-P. (2005), The Palaeozoic evolution of the Maures massif (France) and its potential correlation with others areas of the Variscan belt: a review, *Journal of the virtual explorer*, *19*, doi: 10.3809/jvirtex.2005.00116.

Bolle, O., M. Corsini, H. Diot, O. Laurent, and R. Melis (2023), Late-orogenic evolution of the southern European variscan belt constrained by fabric analysis and dating of the camarat granitic complex and coeval felsic dykes (maures–tanneron massif, SE France), *Tectonics*, *42*(4), e2022TC007,310, doi: 10.1029/2022tc007310.

Borradaile, G. J., and B. Henry (1997), Tectonic applications of magnetic susceptibility and its anisotropy, *Earth-science reviews*, *42*(1-2), 49–93, doi: 10.1016/s0012-8252(96)00044-x.

Borradaile, G. J., and M. Jackson (2010), Structural geology, petrofabrics and magnetic fabrics (AMS, AARM, AIRM), *Journal of structural geology*, *32*(10), 1519–1551, doi: 10.1016/j.jsg.2009.09.006.

Bouchez, J.-L. (2000), Magnetic susceptibility anisotropy and fabrics in granites, *Comptes Rendus de l'Academie des Sciences Series IIA Earth and Planetary Science*, *1*(330), 1–14.

Brune, S. (2014), Evolution of stress and fault patterns in oblique rift systems: 3-D numerical lithospheric-scale experiments from rift to breakup, *Geochemistry, geophysics, geosystems: G(3)*, *15*(8), 3392–3415, doi: 10.1002/2014gc005446.

Buscail, F. (2000), Contribution à La Compréhension Du Problème Géologique et Géodynamique Du Massif Des Maures : Le Métamorphisme Régional Modélisé Dans Le Système KFMASH : Analyse Pargénétique, Chémiographie, Thermobarométrie, Géochronologie Ar / Ar, Ph.D. thesis, Université Montpellier II, Montpellier, France.

Carosi, R., C. Montomoli, M. Tiepolo, and C. Frassi (2012),

Geochronological constraints on post-collisional shear zones in the Variscides of Sardinia (Italy): Post-collisional shear zones in the Variscides of Sardinia, *Terra nova*, *24*(1), 42–51, doi: 10.1111/j.1365-3121.2011.01035.x.

Carosi, R., A. Petroccia, S. Iaccarino, M. Simonetti, A. Langone, and C. Montomoli (2020), Kinematics and timing constraints in a transpressive tectonic regime: The example of the Posada-Asinara shear zone (NE Sardinia, Italy), *Geosciences*, *10*(8), 288, doi: 10.3390/geosciences10080288.

Carreras, J., J. W. Cosgrove, and E. Druguet (2013), Strain partitioning in banded and/or anisotropic rocks: Implications for inferring tectonic regimes, *Journal of structural geology*, *50*, 7–21, doi: 10.1016/j.jsg.2012.12.003.

Cashman, S. M., H. M. Kelsey, C. F. Erdman, H. N. C. Cutten, and K. R. Berryman (1992), Strain Partitioning between Structural Domains in the Forearc of the Hikurangi Subduction Zone, New Zealand, *Tectonics*, *11*(2), 242–257, doi: 10.1029/91TC02363.

Chardon, D., D. Gapais, and F. Cagnard (2009), Flow of ultra-hot orogens: A view from the Precambrian, clues for the Phanerozoic, *Tectonophysics*, *477*(3-4), 105–118, doi: 10.1016/j.tecto.2009.03.008.

Chardon, D., M. Jayananda, and J.-J. Peucat (2011), Lateral Constrictional Flow of Hot Orogenic Crust: Insights from the Neoarchean of South India, Geological and Geophysical Implications for Orogenic Plateaux, *Geochemistry, geophysics, geosystems: G(3)*, *12*(2), doi: 10.1029/2010GC003398.

Chardon, D., M. Aretz, and D. Roques (2020), Reappraisal of Variscan tectonics in the southern French Massif Central, *Tectonophysics*, *787*(228477), 228,477, doi: 10.1016/j.tecto.2020.228477.

Chorowicz, J., and C. Sorlien (1992), Oblique Extensional Tectonics in the Malawi Rift, Africa, *Geological Society of America Bulletin - GEOL SOC AMER BULL*, *104*, 1015–1023, doi: 10.1130/0016-7606(1992)104<1015:OETITM>2.3.CO;2.

Clegg, P., and R. E. Holdsworth (2005), Complex deformation as a result of strain partitioning in transpression zones: an example from the Leinster Terrane, SE Ireland, *Journal of the Geological Society*, *162*(1), 187–202, doi: 10.1144/0016-764903-177.

Corsini, M., and Y. Rolland (2009), Late evolution of the southern European Variscan belt: Exhumation of the lower crust in a context of oblique convergence, *Comptes rendus: Geoscience*, *341*(2-3), 214–223, doi: 10.1016/j.crte.2008.12.002.

Corsini, M., V. Bosse, G. Féraud, A. Demoux, and G. Crevola (2010), Exhumation processes during post-collisional stage in the Variscan belt revealed by detailed 40Ar/39Ar study (Tanneron Massif, SE France), *International journal of earth sciences*, *99*(2), 327–341, doi: 10.1007/s00531-008-0397-x.

Crevola, G. (1977), Etude Petrographique et Structurale de La Partie Orientale Du Massif de Tanneron (Provence Cristalline), Ph.D. thesis, University of Nice, Nice, France.

Cruden, A. R. (1988), Deformation around a Rising Diapir Modeled by Creeping Flow Past a Sphere, *Tectonics*, *7*(5), 1091–1101, doi: 10.1029/TC007i005p01091.

Cruden, A. R. (1990), Flow and fabric development during the diapiric rise of magma, *The journal of geology*, *98*(5), 681–698, doi: 10.1086/629433.

Darrozes, J., M. Moisy, P. Olivier, L. Améglio, and J. Bouchez (1994), Structure magmatique du granite du Sidobre (Tarn, France) : de l'échelle du massif à celle de l'échantillon, *Comptes rendus de l'Academie des Sciences. Serie 2. Fascicule a. Sciences de la terre et des planetes/Earth and planetary sciences. Montrouge*, *318*(2), 243–250.

Das, J. P., K. Bhattacharyya, and M. A. Mamtani (2021), A kinematic approach for investigating magnetic and strain fabrics from constrictional and flattening domains of shear zones in Sikkim Himalayan fold thrust belt, *Journal of structural geology*, *149*(104388), 104,388, doi: 10.1016/j.jsg.2021.104388.

De Paola, N., R. E. Holdsworth, K. J. W. McCaffrey, and M. R. Barchi (2005), Partitioned transtension: an alternative to basin inversion models, *Journal of structural geology*, *27*(4), 607–625, doi: 10.1016/j.jsg.2005.01.006.

Denèle, Y., D. Roques, J. Ganne, D. Chardon, S. Rousse, and P. Barbey (2017), Strike-Slip Metamorphic Core Complexes: Gneiss Domes Emplaced in Releasing Bends, *Geology*, *45*(10), 903–906, doi: 10.1130/G39065.1.

Dewey, J. F. (2002), Transtension in Arcs and Orogens, *International geology review*, *44*(5), 402–439, doi: 10.2747/0020-6814.44.5.402.

Dewey, J. F., R. E. Holdsworth, and R. A. Strachan (1998), Transpression and Transtension Zones, *Geological Society special publication*, *135*(1), 1–14, doi: 10.1144/GSL.SP.1998.135.01.01.

Diener, J. F. A., and Å (2014), The Influence of Melting and Melt Drainage on Crustal Rheology during Orogenesis, *Journal of geophysical research. Solid earth*, *119*(8), 6193–6210, doi: 10.1002/2014JB011088.

Dirks, P. H. G. M., J. S. Zhang, and C. W. Passchier (1997), Exhumation of high-pressure granulites and the role of lower crustal advection in the North China Craton near Datong, *Journal of structural geology*, *19*(10), 1343–1358, doi: 10.1016/s0191-8141(97)00044-8.

Dixon, J. M. (1975), Finite strain and progressive deformation in models of diapiric structures, *Tectonophysics*, *28*(1-2), 89–124, doi: 10.1016/0040-1951(75)90060-8.

Djouadi, M. T., G. Gleizes, E. Ferré, J. L. Bouchez, R. Caby, and A. Lesquer (1997), Oblique magmatic structures of two epizonal granite plutons, Hoggar, Algeria: late-orogenic emplacement in a transcurrent orogen, *Tectonophysics*, *279*(1-4), 351–374, doi: 10.1016/s0040-1951(97)00123-6.

Duchesne, J.-C., J.-P. Liégeois, O. Bolle, J. Vander Auwera, O. Bruguier, D. I. Matukov, and S. A. Sergeev (2013), The fast evolution of a crustal hot zone at the end of a transpressional regime: The Saint-Tropez peninsula granites and related dykes (Maures Massif, SE France), *Lithos*, *162-163*, 195–220, doi: 10.1016/j.lithos.2012.12.019.

Duclaux, G., R. S. Huismans, and D. A. May (2020), Rotation, narrowing, and preferential reactivation of brittle structures during oblique rifting, *Earth and planetary science letters*, *531*(115952), 115,952, doi: 10.1016/j.epsl.2019.115952.

Ebert, A., M. Herwegh, and A. Pfiffner (2007), Cooling induced strain localization in carbonate mylonites within a large-scale shear zone (Glarus thrust, Switzerland), *Journal of structural geology*, *29*(7), 1164–1184, doi: 10.1016/j.jsg.2007.03.007.

Edel, J. B., K. Schulmann, O. Lexa, and J. M. Lardeaux (2018), Late Palaeozoic palaeomagnetic and tectonic

constraints for amalgamation of Pangea supercontinent in the European Variscan belt, *Earth-science reviews*, *177*, 589–612, doi: 10.1016/j.earscirev.2017.12.007.

Faleiros, F. M., B. V. Ribeiro, G. A. C. Campanha, P. A. Cawood, D. I. G. Cabrita, M. T. A. G. Yogi, L. A. Milani, D. V. Lemos-Santos, V. V. Almeida, S. W. O. Rodrigues, I. S. Malta, and A. J. Forero-Ortega (2022), Strain partitioning along Terrane bounding and intraterrane shear zones: Constraints from a long-lived transpressional system in West Gondwana (Ribeira Belt, Brazil), *Lithosphere*, *2021*(Special 6), 2103,213, doi: 10.2113/2022/2103213.

Fernández, R. D., and M. F. Pereira (2017), Strike-Slip Shear Zones of the Iberian Massif: Are They Coeval?, *Lithosphere*, *9*(5), 726–744, doi: 10.1130/L648.1.

Ferranti, L., E. Santoro, M. E. Mazzella, C. Monaco, and D. Morelli (2009), Active transpression in the northern Calabria Apennines, southern Italy, *Tectonophysics*, *476*(1-2), 226–251, doi: 10.1016/j.tecto.2008.11.010.

Ferré, E. C., A. Gébelin, J. L. Till, C. Sassier, and K. C. Burmeister (2014), Deformation and magnetic fabrics in ductile shear zones: A review, *Tectonophysics*, *629*, 179–188, doi: 10.1016/j.tecto.2014.04.008.

Fletcher, J. M., and J. M. Bartley (1994), Constrictional strain in a non-coaxial shear zone: implications for fold and rock fabric development, central mojave metamorphic core complex, california, *Journal of structural geology*, *16*(4), 555–570, doi: 10.1016/0191-8141(94)90097-3.

Fossen, H., and G. C. G. Cavalcante (2017), Shear zones – A review, *Earth-science reviews*, *171*, 434–455, doi: 10.1016/j.earscirev.2017.05.002.

Fossen, H., and B. Tikoff (1993), The deformation matrix for simultaneous simple shearing, pure shearing and volume change, and its application to transpression-transtension tectonics, *Journal of structural geology*, *15*(3-5), 413–422, doi: 10.1016/0191-8141(93)90137-y.

Fossen, H., and B. Tikoff (1998), Extended models of transpression and transtension, and application to tectonic settings, *Geological Society special publication*, *135*(1), 15–33, doi: 10.1144/gsl.sp.1998.135.01.02.

Fossen, H., B. Tikoff, C. Teyssier, and H. Fossen (1994), Strain modeling of transpressional and transtensional deformation, *Norsk geologisk tidsskrift*, *74*(3), 134–145.

Fossen, H., C. Teyssier, and D. L. Whitney (2013), Transtensional folding, *Journal of structural geology*, *56*, 89–102, doi: 10.1016/j.jsg.2013.09.004.

Fossen, H., G. C. G. Cavalcante, R. V. L. Pinheiro, and C. J. Archanjo (2019), Deformation – progressive or multiphase?, *Journal of structural geology*, *125*, 82–99, doi: 10.1016/j.jsg.2018.05.006.

Franke, W., M. P. Doublier, K. Klama, S. Potel, and K. Wemmer (2011), Hot metamorphic core complex in a cold foreland, *International journal of earth sciences*, *100*(4), 753–785, doi: 10.1007/s00531-010-0512-7.

Frassi, C., R. Carosi, C. Montomoli, and R. D. Law (2009), Kinematics and vorticity of flow associated with post-collisional oblique transpression in the Variscan Inner Zone of northern Sardinia (Italy), *Journal of structural geology*, *31*(12), 1458–1471, doi: 10.1016/j.jsg.2009.10.001.

Fréville, K., P. Trap, J. Vanardois, J. Melleton, M. Faure, O. Bruguier, M. Poujol, and P. Lach (2022), Carboniferous-Permian tectono-metamorphic evolution of the Pelvoux Massif (External Crystalline Massif, Western Alps), with discussion on flow kinematics of the Eastern-Variscan Shear Zone, *Bulletin de la Societe Geologique de France*, *193*(1), 13, doi: 10.1051/bsgf/2022008.

Gapais, D. (1989), Shear Structures within Deformed Granites: Mechanical and Thermal Indicators, *Geology*, *17*(12), 1144–1147, doi: 10.1130/0091-7613(1989)017<1144:SSWDGM>2.3.CO;2.

Gapais, D., A. Potrel, N. Machado, and E. Hallot (2005), Kinematics of long-lasting Paleoproterozoic transpression within the Thompson Nickel Belt, Manitoba, Canada: PALEOPROTEROZOIC TRANSPRESSION, *Tectonics*, *24*(3), doi: 10.1029/2004tc001700.

Gapais, D., A. Pelletier, R.-P. Ménot, and J.-J. Peucat (2008), Paleoproterozoic tectonics in the Terre Adélie craton (east Antarctica), *Precambrian research*, *162*(3-4), 531–539, doi: 10.1016/j.precamres.2007.10.011.

Gattacceca, J. (2000), Cinématique Du Bassin Liguro-Provençal Entre 30 et 12 Ma. Implication Géodynamiques, Ph.D. thesis, Paris, ENMP.

Gerbault, M., J. Schneider, A. Reverso-Peila, and M. Corsini (2018), Crustal exhumation during ongoing compression in the Variscan Maures-Tanneron Massif, France-Geological and thermo-mechanical aspects, *Tectonophysics*, *746*, 439–458, doi: 10.1016/j.tecto.2016.12.019.

Ghosh, S. K., D. Khan, and S. Sengupta (1995), Interfering folds in constrictional deformation, *Journal of structural geology*, *17*(10), 1361–1373, doi: 10.1016/0191-8141(95)00027-b.

Giacomini, F., L. Dallai, E. Carminati, M. Tiepolo, and C. Ghezzo (2008), Exhumation of a Variscan orogenic complex: insights into the composite granulitic–amphibolitic metamorphic basement of south-east Corsica (France), *Journal of metamorphic geology*, *26*(4), 403–436, doi: 10.1111/j.1525-1314.2008.00768.x.

Goodwin, L. B., and B. Tikoff (2002), Competency contrast, kinematics, and the development of foliations and lineations in the crust, *Journal of structural geology*, *24*(6-7), 1065–1085, doi: 10.1016/s0191-8141(01)00092-x.

Goodwin, L. B., and P. F. Williams (1996), Deformation path partitioning within a transpressive shear zone, Marble Cove, Newfoundland, *Journal of structural geology*, *18*(8), 975–990, doi: 10.1016/0191-8141(96)00015-6.

Gremmel, J., P. Trap, B. Le Bayon, R. Mumba, T. Fullgraf, and P. Lach (2023), Tectono-metamorphic evolution and strain partitioning along the Mugesse mega shear zone, Ubendian Belt (Northern Malawi), *Journal of African earth sciences (Oxford, England: 1994)*, *205*(104949), 104,949, doi: 10.1016/j.jafrearsci.2023.104949.

Gébelin, A., M. Brunel, P. Monié, M. Faure, and N. Arnaud (2007), Transpressional tectonics and Carboniferous magmatism in the Limousin, Massif Central, France: Structural and $^{40}Ar/^{39}Ar$ investigations: MAGMATISM AND TECTONICS, *Tectonics*, *26*(2), doi: 10.1029/2005tc001822.

Gébelin, A., F. Roger, and M. Brunel (2009), Syntectonic crustal melting and high-grade metamorphism in a transpressional regime, Variscan Massif Central, France, *Tectonophysics*, *477*(3-4), 229–243, doi: 10.1016/j.tecto.2009.03.022.

Handy, M. R. (1990), The solid-state flow of polymineralic rocks, *Journal of geophysical research*, *95*(B6), 8647, doi: 10.1029/jb095ib06p08647.

Handy, M. R. (1994), Flow laws for rocks containing two non-linear viscous phases: A phenomenological approach, *Journal of structural geology*, *16*(3), 287–301, doi: 10.1016/0191-8141(94)90035-3.

Harland, W. B. (1971), Tectonic transpression in Caledonian Spitsbergen, *Geological magazine*, *108*(1), 27–41, doi: 10.1017/s0016756800050937.

Henry, B., N. Merabet, M. E. M. Derder, and B. Bayou (2004), Chemical Remagnetizations in the Illizi Basin (Saharan Craton, Algeria) and Their Acquisition Process, *Geophysical journal international*, *156*(2), 200–212, doi: 10.1111/j.1365-246X.2003.02106.x.

Hrouda, F. (2002), The use of the anisotropy of magnetic remanence in the resolution of the anisotropy of magnetic susceptibility into its ferromagnetic and paramagnetic components, *Tectonophysics*, *347*(4), 269–281, doi: 10.1016/s0040-1951(02)00075-6.

Hunter, N. J. R., P. Hasalová, R. F. Weinberg, and C. J. L. Wilson (2016), Fabric controls on strain accommodation in naturally deformed mylonites: The influence of interconnected micaceous layers, *Journal of structural geology*, *83*, 180–193, doi: 10.1016/j.jsg.2015.12.005.

Jackson, M. (1991), Anisotropy of magnetic remanence: A brief review of mineralogical sources, physical origins, and geological applications, and comparison with susceptibility anisotropy, *Pure and applied geophysics*, *136*(1), 1–28, doi: 10.1007/bf00878885.

Jacob, J.-B., S. Guillot, D. Rubatto, E. Janots, J. Melleton, and M. Faure (2021), Carboniferous high- P metamorphism and deformation in the Belledonne Massif (Western Alps), *Journal of metamorphic geology*, *39*(jmg.12600), 1009–1044, doi: 10.1111/jmg.12600.

Jelinek, V. (1981), Characterization of the magnetic fabric of rocks, *Tectonophysics*, *79*(3-4), T63–T67, doi: 10.1016/0040-1951(81)90110-4.

Jelínek, V. (1978), Statistical processing of anisotropy of magnetic susceptibility measured on groups of specimens, *Studia geophysica et geodaetica*, *22*(1), 50–62, doi: 10.1007/bf01613632.

Ji, S., Z. Jiang, E. Rybacki, R. Wirth, D. Prior, and B. Xia (2004), Strain softening and microstructural evolution of anorthite aggregates and quartz–anorthite layered composites deformed in torsion, *Earth and planetary science letters*, *222*(2), 377–390, doi: 10.1016/j.epsl.2004.03.021.

Jiang, D. (1994a), Vorticity determination, distribution, partitioning and the heterogeneity and non-steadiness of natural deformations, *Journal of structural geology*, *16*(1), 121–130, doi: 10.1016/0191-8141(94)90023-x.

Jiang, D. (1994b), Flow variation in layered rocks subjected to bulk flow of various kinematic vorticities: theory and geological implications, *Journal of structural geology*, *16*(8), 1159–1172, doi: 10.1016/0191-8141(94)90059-0.

Jones, R. R., R. E. Holdsworth, P. Clegg, K. McCaffrey, and E. Tavarnelli (2004), Inclined transpression, *Journal of structural geology*, *26*(8), 1531–1548, doi: 10.1016/j.jsg.2004.01.004.

Klepeis, K. A., J. J. Schwartz, E. Miranda, P. Lindquist, R. Jongens, R. Turnbull, and H. Stowell (2022), The initiation and growth of transpressional shear zones through continental arc lithosphere, southwest New Zealand, *Tectonics*, *41*(9), e2021TC007,097, doi: 10.1029/2021tc007097.

Kruckenberg, S. C., O. Vanderhaeghe, E. C. Ferré, C. Teyssier, and D. L. Whitney (2011), Flow of Partially Molten Crust and the Internal Dynamics of a Migmatite Dome, Naxos, Greece, *Tectonics*, *30*(3), doi: 10.1029/2010TC002751.

Le Pourhiet, L., B. Huet, D. A. May, L. Labrousse, and L. Jolivet (2012), Kinematic Interpretation of the 3D Shapes of Metamorphic Core Complexes, *Geochemistry, geophysics, geosystems: G(3)*, *13*(9), doi: 10.1029/2012GC004271.

Lee, A. L., T. Torvela, G. E. Lloyd, and A. M. Walker (2018), Melt organisation and strain partitioning in the lower crust, *Journal of structural geology*, *113*, 188–199, doi: 10.1016/j.jsg.2018.05.016.

Lister, G. S., and P. F. Williams (1983), The partitioning of deformation in flowing rock masses, *Tectonophysics*, *92*(1-3), 1–33, doi: 10.1016/0040-1951(83)90083-5.

Maillet, A., J. Gremmel, and G. Duclaux (2021), Cartographie et analyse structurale du bassin Carbonifère du Reyran, massif de Tanneron (Maures-Tanneron), doi: 10.13140/RG.2.2.22163.25122/1.

Meghraoui, M., and S. Pondrelli (2013), Active faulting and transpression tectonics along the plate boundary in North Africa, *Annals of geophysics*, *55*(5), 955–967, doi: 10.4401/ag-4970.

Montési, L. G. J. (2013), Fabric development as the key for forming ductile shear zones and enabling plate tectonics, *Journal of structural geology*, *50*, 254–266, doi: 10.1016/j.jsg.2012.12.011.

Morley, C. K., C. Haranya, W. Phoosongsee, S. Pongwapee, A. Kornsawan, and N. Wonganan (2004), Activation of rift oblique and rift parallel pre-existing fabrics during extension and their effect on deformation style: examples from the rifts of Thailand, *Journal of structural geology*, *26*(10), 1803–1829, doi: 10.1016/j.jsg.2004.02.014.

Mount, V. S., and J. Suppe (1992), Present-day stress orientations adjacent to active strike-slip faults: California and Sumatra, *Journal of geophysical research*, *97*(B8), 11,995, doi: 10.1029/92jb00130.

Norris, R. J., P. O. Koons, and A. F. Cooper (1990), The obliquely-convergent plate boundary in the South Island of New Zealand: implications for ancient collision zones, *Journal of structural geology*, *12*(5-6), 715–725, doi: 10.1016/0191-8141(90)90084-c.

Nédélec, A., and J.-L. Bouchez (2015), *Granites: Petrology, structure, geological setting, and metallogeny*, OUP Oxford.

Oldow, J. S., A. W. Bally, and H. G. Avé Lallemant (1990), Transpression, Orogenic Float, and Lithospheric Balance, *Geology*, *18*(10), 991–994, doi: 10.1130/0091-7613(1990)018<0991:TOFALB>2.3.CO;2.

Oliot, E., J. Melleton, J. Schneider, M. Corsini, V. Gardien, and Y. Rolland (2015), Variscan crustal thickening in the Maures-Tanneron massif (South Variscan belt, France): new in situ monazite U-Th-Pb chemical dating of high-grade rocks, *Bulletin de la Societe Geologique de France*, *186*(2-3), 145–169, doi: 10.2113/gssgfbull.186.2-3.145.

Onézime, J., M. Faure, and G. Crévola (1999), Étude pétro-structurale du complexe granitique Rouet — Plan-de-la-Tour (massifs des Maures et du Tanneron occidental, Var), *Comptes rendus de l'Academie des*

Sciences. Serie 2. Fascicule a. Sciences de la terre et des planetes/Earth and planetary sciences. Montrouge, *328*(11), 773–779, doi: 10.1016/s1251-8050(99)80170-0.

Orsini, J.-B. (1968), Etude pétrographique et structurale du Massif du Tanneron (Var)-Parties occidentale et centrale, Ph.D. thesis, Université de Grenoble.

Passchier, C. W., and R. A. J. Trouw (2005), *Microtectonics*, Springer-Verlag, Berlin/Heidelberg, doi: 10.1007/3-540-29359-0.

Paulsen, T. S., J. EncarnaciÓn, and A. M. Grunow (2004), Structure and timing of transpressional deformation in the Shackleton Glacier area, Ross orogen, Antarctica, *Journal of the Geological Society*, *161*(6), 1027–1038, doi: 10.1144/0016-764903-040.

Rabin, M., P. Trap, N. Carry, K. Fréville, B. Cenki-Tok, C. Lobjoie, P. Goncalves, and D. Marquer (2015), Strain partitioning along the anatectic front in the Variscan Montagne Noire massif (southern French Massif Central): Anatectic Front and Strain Partitioning, *Tectonics*, *34*(8), 1709–1735, doi: 10.1002/2014tc003790.

Rey, P. F., L. Mondy, G. Duclaux, C. Teyssier, D. L. Whitney, M. Bocher, and C. Prigent (2017), The origin of contractional structures in extensional gneiss domes, *Geology*, *45*(3), 263–266, doi: 10.1130/g38595.1.

Richard, P. D., M. A. Naylor, and A. Koopman (1995), Experimental models of strike-slip tectonics, *Petroleum geoscience*, *1*(1), 71–80, doi: 10.1144/petgeo.1.1.71.

Roberts, N. M., and B. Tikoff (2021), Internal structure of the Paleoarchean Mt Edgar dome, Pilbara Craton, Western Australia, *Precambrian research*, *358*(106163), 106,163, doi: 10.1016/j.precamres.2021.106163.

Rochette, P. (1987), Magnetic susceptibility of the rock matrix related to magnetic fabric studies, *Journal of structural geology*, *9*(8), 1015–1020, doi: 10.1016/0191-8141(87)90009-5.

Rochette, P., M. Jackson, and C. Aubourg (1992), Rock Magnetism and the Interpretation of Anisotropy of Magnetic Susceptibility, *Reviews of geophysics (Washington, D.C.: 1985)*, *30*(3), 209–226, doi: 10.1029/92RG00733.

Rolland, Y., M. Corsini, and A. Demoux (2009), Metamorphic and structural evolution of the Maures-Tanneron massif (SE Variscan chain): evidence of doming along a transpressional margin, *Bulletin de la Societe Geologique de France*, *180*(3), 217–230, doi: 10.2113/gssgfbull.180.3.217.

Rutter, E. H., R. E. Holdsworth, and R. J. Knipe (2001), The Nature and Tectonic Significance of Fault-Zone Weakening: An Introduction, *Geological Society, London, Special Publications*, *186*(1), 1–11, doi: 10.1144/GSL.SP.2001.186.01.01.

Sanderson, D. J., and W. R. D. Marchini (1984), Transpression, *Journal of structural geology*, *6*(5), 449–458, doi: 10.1016/0191-8141(84)90058-0.

Schneider, J., M. Corsini, A. Reverso-Peila, and J.-M. Lardeaux (2014), Thermal and mechanical evolution of an orogenic wedge during Variscan collision: an example in the Maures–Tanneron Massif (SE France), *Geological Society special publication*, *405*(1), 313–331, doi: 10.1144/sp405.4.

Schreurs, G., and B. Colletta (1998), Analogue modelling of faulting in zones of continental transpression and transtension, *Geological Society special publication*, *135*(1), 59–79, doi: 10.1144/gsl.sp.1998.135.01.05.

Shan, Y. (2008), An analytical approach for determining strain ellipsoids from measurements on planar surfaces, *Journal of structural geology*, *30*(4), 539–546, doi: 10.1016/j.jsg.2006.12.004.

Shea, W. T., Jr, and A. K. Kronenberg (1993), Strength and anisotropy of foliated rocks with varied mica contents, *Journal of structural geology*, *15*(9-10), 1097–1121, doi: 10.1016/0191-8141(93)90158-7.

Simonetti, M., R. Carosi, C. Montomoli, A. Langone, E. D'Addario, and E. Mammoliti (2018), Kinematic and geochronological constraints on shear deformation in the Ferriere-Mollières shear zone (Argentera-Mercantour Massif, Western Alps): implications for the evolution of the Southern European Variscan Belt, *International journal of earth sciences*, *107*(6), 2163–2189, doi: 10.1007/s00531-018-1593-y.

Simonetti, M., R. Carosi, C. Montomoli, M. Corsini, A. Petroccia, J. M. Cottle, and S. Iaccarino (2020a), Timing and kinematics of flow in a transpressive dextral shear zone, Maures Massif (Southern France), *Geologische Rundschau: Zeitschrift fur allgemeine Geologie*, *109*(7), 2261–2285, doi: 10.1007/s00531-020-01898-6.

Simonetti, M., R. Carosi, C. Montomoli, J. M. Cottle, and R. D. Law (2020b), Transpressive deformation in the southern European variscan belt: New insights from the aiguilles rouges massif (western alps), *Tectonics*, *39*(6), e2020TC006,153, doi: 10.1029/2020tc006153.

Skyttä, P., T. Hermansson, S.-Å. Elming, and T. Bauer (2010), Magnetic fabrics as constraints on the kinematic history of a pre-tectonic granitoid intrusion, Kristineberg, northern Sweden, *Journal of structural geology*, *32*(8), 1125–1136, doi: 10.1016/j.jsg.2010.06.020.

Stipp, M., H. Stünitz, R. Heilbronner, and S. M. Schmid (2002), Dynamic Recrystallization of Quartz: Correlation between Natural and Experimental Conditions, *Geological Society, London, Special Publications*, *200*(1), 171–190, doi: 10.1144/GSL.SP.2001.200.01.11.

Stuart, C. A., S. Piazolo, and N. R. Daczko (2018), The recognition of former melt flux through high-strain zones, *Journal of metamorphic geology*, *36*(8), 1049–1069, doi: 10.1111/jmg.12427.

Sullivan, W. A. (2006), Structural significance of L tectonites in the Eastern-central Laramie mountains, Wyoming, *The journal of geology*, *114*(5), 513–531, doi: 10.1086/506158.

Sullivan, W. A. (2008), Significance of transport-parallel strain variations in part of the Raft River shear zone, Raft River Mountains, Utah, USA, *Journal of structural geology*, *30*(2), 138–158, doi: 10.1016/j.jsg.2007.11.007.

Sullivan, W. A. (2013), L tectonites, *Journal of structural geology*, *50*, 161–175, doi: 10.1016/j.jsg.2012.01.022.

Sylvester, A. G., and R. Robert (1976), Tectonic transpression and basement-controlled deformation in San Andreas fault zone, Salton trough, California, *AAPG bulletin*, *60*(12), 2081–2102, doi: 10.1306/c1ea3a73-16c9-11d7-8645000102c1865d.

Talbot, C. J., and M. P. A. Jackson (1987), Internal kinematics of salt diapirs, *AAPG bulletin*, *71*(9), 1068–1093, doi: 10.1306/703c7df9-1707-11d7-8645000102c1865d.

Teyssier, C., and B. Tikoff (1998), Strike-slip partitioned transpression of the San Andreas fault system: a lithospheric-scale approach, *Geological Society special publication*, *135*(1), 143–158, doi: 10.1144/gsl.sp.1998.135.01.10.

Teyssier, C., and B. Tikoff (1999), Fabric stability in oblique

convergence and divergence, *Journal of structural geology*, *21*(8-9), 969–974, doi: 10.1016/s0191-8141(99)00067-x.

Teyssier, C., B. Tikoff, and M. Markley (1995), Oblique Plate Motion and Continental Tectonics, *Geology*, *23*, doi: 10.1130/0091-7613(1995)023<0447:OPMACT>2.3.CO;2.

Thevoux-Chabuel, H., R. Menot, J. Lardeaux, and O. Monnier (1995), Evolution tectono-métamorphique polyphasée paléozoïque dans le socle de Zicavo (Corse-du-Sud): témoin d'un amincissement post-orogénique, *Comptes rendus de l'Academie des Sciences. Serie 2. Fascicule a. Sciences de la terre et des planetes/Earth and planetary sciences. Montrouge*, *321*(1), 47–56.

Tikoff, B., and C. Teyssier (1994), Strain modeling of displacement-field partitioning in transpressional orogens, *Journal of structural geology*, *16*(11), 1575–1588, doi: 10.1016/0191-8141(94)90034-5.

Toutin-Morin, N., G. Crevola, J. D. Giraud, M. Dubar, C. Brocard, G. Dardeau, P. F. Bulard, A. Meinesz, and D. Bonijoly (1994), Carte Géologique de La France à 1/50 000, Feuille 1024 Fréjus-Cannes.

Umhoefer, P. J., and R. J. Dorsey (1997), Translation of Terranes: Lessons from Central Baja California, Mexico, *Geology*, *25*(11), 1007–1010, doi: 10.1130/0091-7613(1997)025<1007:TOTLFC>2.3.CO;2.

Vanardois, J. (2021), Fusion Partielle, Transfert de Magma et Partitionnement de La Déformation Au Cours de l'orogénèse Varisque : Exemple Des Massifs Des Aiguilles-Rouges (Alpes) et de l'Agly (Pyrénées), Ph.D. thesis, Bourgogne Franche-Comté.

Vanardois, J., P. Trap, P. Goncalves, D. Marquer, J. Gremmel, G. Siron, and T. Baudin (2020), Kinematics, deformation partitioning and late Variscan magmatism in the Agly massif, Eastern Pyrenees, France, *Bulletin de la Societe Geologique de France*, *191*(1), 15, doi: 10.1051/bsgf/2020009.

Vanardois, J., P. Trap, F. Roger, J. Melleton, D. Marquer, J.-L. Paquette, P. Goncalves, F. Cagnard, and B. Le Bayon (2022), Deformation, crustal melting and magmatism in the crustal-scale East-Variscan Shear Zone (Aiguilles-Rouges and Mont-Blanc massifs, Western Alps), *Journal of structural geology*, *163*(104724), 104,724, doi: 10.1016/j.jsg.2022.104724.

Vauchez, P. A., and M. Bufalo (1988), Charriage crustal, anatexie et decrochements ductiles dans les Maures orientales (Var, France) au cours de l'orogenese varisque, *International journal of earth sciences*, *77*(1), 45–62, doi: 10.1007/bf01848675.

Vollmer, F. W. (2018), Automatic contouring of geologic fabric and finite strain data on the unit hyperboloid, *Computers & geosciences*, *115*, 134–142, doi: 10.1016/j.cageo.2018.03.006.

Wiest, J. D., P. T. Osmundsen, J. Jacobs, and H. Fossen (2019), Deep crustal flow within postorogenic metamorphic core complexes: Insights from the southern western gneiss region of Norway, *Tectonics*, *38*(12), 4267–4289, doi: 10.1029/2019tc005708.

Wilson, R. W., K. J. W. McCaffrey, R. E. Holdsworth, J. Imber, R. R. Jones, A. I. F. Welbon, and D. Roberts (2006), Complex Fault Patterns, Transtension and Structural Segmentation of the Lofoten Ridge, Norwegian Margin: Using Digital Mapping to Link Onshore and Offshore Geology, *Tectonics*, *25*(4), doi: 10.1029/2005TC001895.

Wintsch, R. P., R. Christoffersen, and A. K. Kronenberg (1995), Fluid-rock reaction weakening of fault zones, *Journal of geophysical research*, *100*(B7), 13,021–13,032, doi: 10.1029/94jb02622.

Withjack, M. O., and W. R. Jamison (1986), Deformation produced by oblique rifting, *Tectonophysics*, *126*(2-4), 99–124, doi: 10.1016/0040-1951(86)90222-2.

Zibra, I., J. H. Kruhl, A. Montanini, and R. Tribuzio (2012), Shearing of magma along a high-grade shear zone: Evolution of microstructures during the transition from magmatic to solid-state flow, *Journal of structural geology*, *37*, 150–160, doi: 10.1016/j.jsg.2012.01.011.